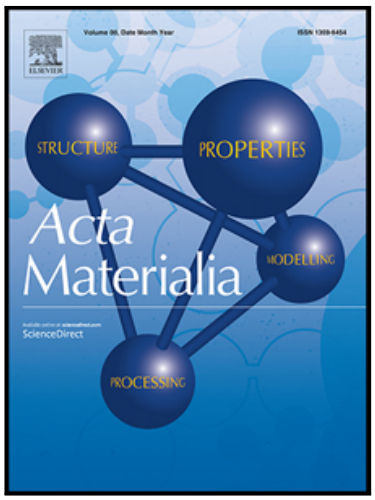

NiTiCu Shape Memory Alloys with Ultra-Low Phase Transformation Range as Solid-State Phase Change Materials

W. Trehern , N. Hite , R. Ortiz-Ayala , K.C. Atli , D.J. Sharar , A.A. Wilson , R. Seede , A.C. Leff , I. Karaman

PII: S1359-6454(23)00640-7
DOI: https://doi.org/10.1016/j.actamat.2023.119310
Reference: AM 119310

To appear in: *Acta Materialia*

Received date: 1 July 2023
Revised date: 28 August 2023
Accepted date: 30 August 2023

Please cite this article as: W. Trehern , N. Hite , R. Ortiz-Ayala , K.C. Atli , D.J. Sharar , A.A. Wilson , R. Seede , A.C. Leff , I. Karaman , NiTiCu Shape Memory Alloys with Ultra-Low Phase Transformation Range as Solid-State Phase Change Materials, *Acta Materialia* (2023), doi: https://doi.org/10.1016/j.actamat.2023.119310

Submitted to Acta Materialia in June 2023, Revised in August 2023

NiTiCu Shape Memory Alloys with Ultra-Low Phase Transformation Range as Solid-State Phase Change Materials

W. Trehern[a,1], N. Hite[a,1], R. Ortiz-Ayala[a], K.C. Atli[a], D.J. Sharar[b], A.A. Wilson[b], R. Seede[a], A.C. Leff[b,c], I. Karaman[a,*]

[a]Department of Materials Science and Engineering, Texas A&M University, College Station, TX, USA
[b]U.S. Army Research Laboratory, Adelphi MD, USA
[c]General Technical Services, LLC, Wall, NJ, USA

[1]Equal contribution
*Corresponding author: ikaraman@tamu.edu

Abstract

Shape memory alloys (SMAs) have been demonstrated as effective phase change materials (PCMs) for thermal energy storage (TES) applications. NiTi and NiTiHf SMAs have shown high TES performance, as quantified by PCM figure of merit (FOM) but their use in applications requiring narrow operation temperature windows is limited by large overall phase transformation ranges (OTR). This work investigates NiTiCu SMAs as PCMs with high FOM and low OTR. A full-factorial design of experiments is used to examine 24 NiTiCu compositions. The compositions were fabricated using vacuum arc melting and their phase transformation and thermophysical properties were characterized using calorimetry, thermal diffusivity, and density measurements. The NiTiCu compositions spanned martensitic transformation temperatures between -22 °C and 84 °C and exhibited greater FOM (250-1050 $10^6 J^2K^{-1}s^{-1}m^{-4}$), compared to traditional PCMs (typically <100 $10^6 J^2K^{-1}s^{-1}m^{-4}$), with major benefits associated with higher density and higher thermal conductivity values. In addition, the NiTiCu compositions in this study show ultra-low OTR (12-20 °C) compared to NiTi and NiTiHf SMAs (>50 °C), enabling utility in narrow operating temperature windows. Thermal cycling was also performed revealing extreme stability of martensitic transformation with only 0.04 °C shift in transformation temperatures after 80 thermal cycles, which is the lowest reported to date in SMA literature.

Keywords: Shape Memory Alloys; Thermal Energy Storage; Cyclic Stability; Phase Change Materials; Thermal Conductivity.

1. Introduction

Shape memory alloys (SMAs) have recently been demonstrated as effective solid-to-solid phase change materials (PCMs) in thermal energy storage (TES) and thermal management applications [1-3]. The endothermic reverse martensitic transformation of SMAs allows them to function similarly to traditional solid-to-liquid PCMs, absorbing large amounts of heat while maintaining nearly constant temperature. This is demonstrated in Fig. 1 which depicts a characteristic heat flow vs. temperature curve of a PCM undergoing melting and recrystallization, or equivalently, an SMA undergoing reverse and forward martensitic phase transformation in an example thermal management application (e.g., an electronic chip). At Step 1, the system operates at steady state, with the waste heat from the electronic chip being dissipated by conduction through the PCM/SMA and subsequently by convection to the surrounding air. When the power supplied to the chip is increased during Step 2, heat flow into the PCM/SMA is increased, causing it to undergo sensible heating. At the beginning of Step 3, the PCM reaches its melting onset temperature (austenite start temperature – A_s – for SMAs) and the rate of the temperature increase decreases significantly due to the latent heat absorbed by the PCM (often referred to as transformation enthalpy within the context of SMAs). As the PCM continues to absorb heat from the electronic chip, its temperature remains relatively constant until the latent heat is exhausted and the melting endpoint temperature (austenite finish temperature – A_f – for SMAs) is reached. At this point, a traditional PCM is fully in the liquid phase, and a SMA is fully in the austenite phase. During Step 4, the power supplied to the chip is reduced to its baseline level, allowing the PCM/SMA to cool sensibly until it reaches its crystallization onset temperature (martensite start temperature – M_s – for SMAs). As the PCM continues to transfer its stored thermal energy to the surroundings, it reaches its crystallization endpoint temperature (martensite finish temperature – M_f – for SMAs), "resetting" the phase transformation. At this point, a traditional PCM has fully transformed back to the solid phase, and an SMA has fully transformed back to the martensite phase. The chip can then operate at steady state until high-power operation is again needed, at which time the cycle is repeated. In this way, PCM/SMAs can be used to reduce maximum temperatures experienced during power spikes as shown in the inset in the corner of Fig. 1, and as demonstrated experimentally by Sharar et al. [1].

Traditional organic and inorganic PCMs have been used in many TES and thermal management applications including building temperature regulation, solar air and water heating systems, battery thermal management, space applications, and microelectronic thermal management [4-7]. The viability of PCMs in the aforementioned applications is due to low-cost, high thermal capacitance, and thermal energy storage with minimal weight and volume [8]. In an example application with a produced thermal energy of 225 kJ, a 1 kg aluminum heat sink would be heated by 250 °C to absorb the heat through sensible heating, whereas 1 kg of 1-Octadecanol (a traditional organic PCM with a heat of fusion of 225 $kJkg^{-1}$ and a melting

temperature of ~58 °C) or paraffin (with a heat of fusion of 200 $kJkg^{-1}$ and a melting temperature of ~130 °C)) could be heated sensibly and then melted to absorb the remaining heat through an endothermic phase change [2]. Despite the many uses of traditional PCMs, low thermal conductivity, typically ranging from 0.1 to 0.7 $Wm^{-1}K^{-1}$ [9], limits their use in applications where fast transient thermal transport is required (for example, microelectronic thermal management as depicted in Fig. 1). By comparison, SMAs have thermal conductivity values 1-2 orders of magnitude greater than traditional PCMs, with values ranging from 12-18 $Wm^{-1}K^{-1}$ [2, 10, 11], making them good candidates for such applications.

In order to identify the optimal PCM for fast transient thermal management applications, Lu [12] derived a figure of merit (FOM) criterion, which solves the Neumann-Stefan problem for melting of a semi-infinite material, quantifying the ability of a PCM to absorb a heat pulse as $\mathrm{FOM} = \rho \cdot L \cdot k$, where k is the thermal conductivity, L is the latent heat of transformation, and ρ is the density of the high temperature phase (austenite or liquid) (see also Shamberger [13] and Shao et al. [14]). A high value of FOM is desirable for PCMs because it represents a material's ability to rapidly store and release large quantities of thermal energy in a small volume. $\rho \cdot L$ defines the volumetric energy storage capacity, while k determines the rate at which thermal energy can travel from the heat source, through the transformed material, i.e., austenite, to the phase front within the PCM. FOM applies to any material exhibiting endothermic phase transitions upon heating and has recently been used to demonstrate the superiority of SMAs for high power (or short time-response) thermal energy storage applications. While typically not explicitly reported, these material properties are important in standard use cases of materials exhibiting reversible martensitic transformations (such as shape memory actuation and elastocaloric cooling). Optimization for these uses requires careful consideration of thermal conductivity and heat capacity to control work input, cooling work, and thermal time constant. Therefore, FOM and constituent properties are good indicators of the behavior of materials exhibiting reversible martensitic transformations.

It has been shown that NiTi [1] and NiTiHf [3] SMAs, in part due to their relatively high thermal conductivities, have FOM values an order of magnitude greater than those of traditional PCMs, making SMAs preferable in high-heat flux thermal management and thermal storage applications. Furthermore, in contrast to traditional PCMs such as salt hydrates, polymers, paraffin, and other organics, SMAs remain solid throughout their transformation, eliminating the need for fluid containment as is necessary for traditional solid-to-liquid PCMs. In recent works, the thermal conductivities of traditional PCMs have been increased by adding a conductive dispersed phase [15-18], however the FOM values of these composite PCMs are typically less than 800 $10^6 J^2K^{-1}s^{-1}m^{-4}$[15-18] compared to SMAs which have FOM values ranging up to 3200 $10^6 J^2K^{-1}s^{-1}m^{-4}$[1-3]. The implementation of composite PCMs is further hindered by difficult fabrication procedures and the need for containment of the liquid phase which adds size and weight to the

system which does not directly contribute to the thermal energy storage process. Traditional solid-to-solid PCMs show even lower FOM values, typically less than 140 $10^6 J^2K^{-1}s^{-1}m^{-4}$[9].

Despite the advantages provided by the high FOM values and solid-to-solid transformations of NiTi and NiTiHf SMAs, both alloys have large overall transformation range (OTR, calculated by A_f-M_f) in excess of 50 °C, excluding them from some applications [3, 19]. As an example, some solid-state lasers may be limited to operation temperature ranges as narrow as 10 °C, and therefore corresponding PCM thermal management solutions must undergo full forward and reverse transformations within these narrow temperature windows [20]. Solid-to-solid PCMs can also be used as energy harvesters from low-grade heat sources (hot-side temperature <50 °C) where current thermal energy harvesting technologies, primarily thermoelectric generators, have too low of efficiency to be cost-effective. SMAs with low transformation temperatures and OTR can efficiently harness the abundant low temperature gradients (<10 °C), thereby, opening the possibility to implement self-powered sensors in variety of scenarios [21]. Regardless of application temperature range requirements, lower OTRs in PCMs are preferable because they allow for increased thermal cycling frequency and therefore a higher number of heat pulses can be absorbed within a given length of time. Low OTRs are especially important in SMAs in thermal cycling applications, as observed latent heat is maximized with complete austenite and martensite transformation. Furthermore, the temperature memory of SMAs degrades with partial cycling, which could lead the operating temperature of the SMA to shift outside of the objective temperature range [22, 23]. Thus, to optimize an SMA for thermal storage and management applications, minimization of the OTR is necessary to ensure transformation is completed within the application temperature constraints. Therefore, an evaluation of the material parameters affecting OTR and transformation temperatures is needed.

While OTR in SMAs is a function of frictional resistance to interfacial motion similar to thermal hysteresis, it is also a function of the elastic strain energy stored during martensitic transformation and its dissipation [24]. By reducing the density of defects in an SMA, the frictional resistance to motion of transforming phases can be decreased. To minimize the dissipation of the stored elastic strain energy, the crystallographic compatibility between martensite and austenite phases must be improved [25]. Based on the geometric nonlinear theory of martensite, crystallographic compatibility can be qualitatively described by the middle eigenvalue (λ_2) of the transformation stretch tensor between austenite and martensite lattices. The closer λ_2 is to a value of 1, the better the compatibility between the austenite-martensite interfaces during transformation and thus the lower chance of defect formation [25-30]. Finally, reducing the amount of stored elastic strain energy can be accomplished by reducing defect density and precipitate coherency strains [24]. In the absence of defects such as dislocations and precipitates, martensitic transformation is nucleation controlled, propagating instantly through the material upon reaching critical nuclei size [31].

Chemical homogeneity throughout a sample is also important as the transformation temperatures are sensitive to small changes in composition [19]. Chemical homogeneity will ensure the martensitic transformation to occur at a given temperature simultaneously throughout the entirety of the material within a narrow temperature range.

In NiTi-based SMAs, Cu, Pd, Au, and Cr elemental additions can result in a smaller OTR than other NiTi-based SMAs [25, 27, 32-37], and of these elemental additions, Cu and Pd have the greatest effect on minimizing the OTR [30, 32, 35, 36, 38-40] due to the change in the martensite crystal structure and enhanced crystallographic compatibility. However, the composition and processing parameters in a given NiTi-X system can greatly affect the observed OTR. These differences can be seen in NiTiCu alloys as shown by the adapted DSC plots from literature in Fig. 2A. To further illustrate the effect of composition and processing parameters on overall transformation range (OTR) and peak offset, DSC plots of selected NiTi, NiTiPd, and NiTiHf SMAs are shown in Fig. 3. The offset of martensite and austenite peaks, characterized by A_s-M_s, and the entire OTR, A_f-M_f, is used to determine candidate alloys, shown in Fig. 2B. The smallest OTRs occur in compositions that are capable of single step B2-B19 phase transformations (more commonly reported in NiTiCu and NiTiPd SMAs), rather than B2-B19' (more commonly reported in NiTi and NiTiHf SMAs) or multi-step B2-B19-B19' phase transformations. To achieve the minimum OTR, the ideal SMA would have characteristically sharp martensite and austenite DSC peaks that have minimal peak offset, indicating both austenite and martensite phase transformations occur rapidly with temperature change and within the same temperature range throughout the sample. According to Fig. 2B, the smallest OTR can be achieved by reducing the peak offset through altering composition and processing parameters. From Fig. 2B, the candidate alloys are predominately NiTiCu SMA compositions.

To this end, the present work focuses on determining and optimizing the potential TES capacity of the NiTiCu SMA system by synthesizing 24 NiTiCu alloys that have not been systematically studied before, changing Ni and Cu content to investigate the effect of composition on martensitic transformation temperatures and the OTR in bulk samples. The NiTiCu system has been heavily studied for alloys where Ti is near or greater than 50 at. % [30, 41], however, little has been presented for bulk NiTiCu with Ti less than 50 at. % [42]. The effect of Ni and Cu concentration on secondary phase formation is also studied here to better understand the microstructural evolution and its effects on martensitic transformation, thermophysical properties, and PCM performance. In comparison to traditional solid-to-liquid PCMs, solid-to-solid phase transformations in SMAs with small OTRs will offer a unique solution for TES and thermal management applications.

2. Experimental Methods:

The materials with the nominal compositions in Table 1 were fabricated using vacuum arc melting (VAC) using high purity raw materials (>99.99%) to create 12 g buttons. The samples were flipped and remelted at high current 5 times to ensure homogeneity. The buttons were then sealed in quartz tubes under high vacuum, homogenized at 925 °C for 48 h, and air cooled to room temperature. The buttons were then cut via wire electrical discharge machining (wire-EDM) to produce 8 mm diameter x 1 mm thick samples for thermal diffusivity measurement, and 3 mm diameter x 1 mm thick samples were cut for differential scanning calorimetry (DSC) and scanning electron microscopy (SEM). The specimens were polished prior to testing and imaging to remove the possible effects of an EDM recast layer.

A TA Instruments Q2000 differential scanning calorimeter (DSC) was used to determine the stress-free phase transformation temperatures of the arc melted buttons (with a temperature precision of ± 0.01 °C). The material was thermally cycled 3 times at a heating-cooling rate of 10 °C/min, with selected compositions cycled 80 times to determine cyclic stability of the martensitic transformation characteristics. Stress-free transformation temperatures were determined from the DSC peaks using the slope line extension method as described in ASTM F2004-17 [43]. The latent heat of transformation was also calculated from the area under the transformation peaks. The microstructure of the samples was observed using FEI Quanta 600 FE-SEM with a voltage of 15 kV. Oxford energy dispersive X-ray spectroscopy (EDS) system equipped with X-ray mapping and digital imaging was used to determine the composition of the matrix and the second phases present in the material.

Cross-sectional transmission electron microscopy (TEM) samples were prepared using a ThermoFisher Helios G4 UX dual-beam focused ion beam-SEM (FIB-SEM). The phases present in each alloy were identified using SEM-backscatter imaging and regions containing all visible phases were then lifted out using the conventional FIB lift-out technique. TEM characterization was performed using a probe-corrected JEOL ARM200F operated at 200 kV and equipped with an Oxford X-Max TLE 100 mm^2 windowless EDS detector. Specimens were heated in situ in the TEM using a Gatan 652 double-tilt heating stage to transform the martensite to austenite since all of the alloys selected were martensite at room temperature.

Thermal diffusivity was measured using a TA Instruments DXF 200 high-speed Xenon-pulse delivery source and solid-state PIN detector, with measurements taken at approximately 25 °C intervals. Specific heat capacity measurements were extracted from the DSC heat flow data using the sapphire standard method. Finally, thermal conductivity was calculated according to $k(T) = \rho \cdot c_p(T) \cdot \alpha(T)$ where k is temperature dependent thermal conductivity, ρ is density, $c_p(T)$ is temperature dependent specific heat capacity, and $\alpha(T)$ is temperature dependent thermal diffusivity. The density of each alloy was determined

by Archimedes' method, using the sample weight in air and submerged in water of a known temperature according to the equation $\rho = \rho_w * \frac{w_a}{w_a - w_s}$ where ρ is the sample density, ρ_w is the density of water, w_a is the weight of the sample in air, and w_s is the apparent weight of the sample while submerged in water.

3. Results

In order to evaluate the NiTiCu system for various application temperatures, 24 NiTiCu samples were synthesized using a full-factorial design of experiments to investigate the combinatorial $Ni_{100-x-y}Ti_xCu_y$ (at. %) composition space, where x = (40, 42, 44, 46, 48, 50) and y = (20, 22.5, 25, 30). Ti-lean side of the stoichiometry was selected for this study as Ti-lean compositions are capable of forming $(Cu, Ni)_2Ti$ precipitates [44] which, similar to $(Ti, Cu)_2Ni$ precipitates, may be exploited to optimize shape memory properties such as OTR and cyclic stability [45, 46]. In addition, our recent work on data-driven discovery of the lowest transformation hysteresis SMAs under stress, using machine learning and our SMA database, demonstrated the Ti-lean NiTiCu SMA compositions to consistently yield very low hysteresis values [47]. Therefore, these 24 compositions were selected to systematically study the Ti-lean side of the stoichiometry. The compositional space explored in this study is visualized in the ternary diagram in Fig. 4. The 24 alloys have high Cu content (>20 at. %), where, based on a previous study [48], the expected transformation in these alloys is single stage B2 (cubic) to B19 (orthorhombic) martensitic transformation.

After fabrication and homogenization heat treatment of the 24 NiTiCu samples, the microstructures were studied using SEM and TEM. A representative microstructure of NiTiCu samples characterized in this study can be seen in Fig. 5. The compositions of the martensitically transforming NiTiCu matrix, $(Cu, Ni)_2Ti$ and $Ti_2(Cu, Ni)$ second phases were confirmed using EDX. Second phase particles were found to have an ellipsoid morphology in sizes ranging from a few up to tens of micrometers. The second phase $(Cu,Ni)_2Ti$, was only observed in alloys where Ti<50 at. % in agreement with the NiTiCu phase diagram [44]. The composition distributions from EDX can be found Figs. 6A and 6B. The EDX Ti content shows little variation among the three phases of interest (Fig. 6A). Ni and Cu contents vary with respect to each other, and these variations are shown for the transforming matrix and for the second phase (Fig. 6B).

Three Ti-lean compositions with varying Ni content (i.e., $Ni_{27}Ti_{48}Cu_{25}$, $Ni_{29}Ti_{46}Cu_{25}$ and $Ni_{33}Ti_{42}Cu_{25}$) and two equiatomic compositions (i.e., $Ni_{20}Ti_{50}Cu_{30}$ and $Ni_{30}Ti_{50}Ni_{20}$) were further studied via TEM imaging, selected area diffraction patterns (SADP), scanning TEM (STEM)-EDS and STEM-high angle annular dark field (HAADF) imaging. As expected, the NiTiCu matrix was the orthorhombic B19 martensite phase for all compositions. Fig. 7A and 7B display the interface between the B19 martensite and the Ti-rich $Ti_2(Cu, Ni)$ phase in $Ni_{20}Ti_{50}Cu_{30}$. The B19 phase had a much lower density of twins than what is typically observed in B19' martensite. A periodic array of twins with an average spacing of 700 nm and 286 nm was observed for $Ni_{20}Ti_{50}Cu_{30}$ (Fig. 7D) and $Ni_{27}Ti_{48}Cu_{25}$ (Fig. 8F), respectively, while in binary NiTi the spacing is typically on the order of 10 nm (Fig. 7E). There were no nano-scale precipitates found within the B19 matrix.

All the compositions examined except for the $Ni_{20}Ti_{50}Cu_{30}$ alloy had a secondary phase $Ti_2(Cu, Ni)$ with the approximate stoichiometry of Ti_6Ni_2Cu. This phase has the well-known cubic Ti_2Ni crystal structure (space group 227: Fd-3m) (Fig. 8E) that is common in Ti-rich NiTi. The fact that this phase had approximately the same composition across all the alloys in which it was found indicates that the saturation of Cu in the Ti_2Ni phase is likely at ~11 at. %. The $Ni_{20}Ti_{50}Cu_{30}$ alloy also contained a Ti-rich second phase but it had a composition of $Ti_{68.6}Ni_{5.8}Cu_{25.6}$ (at. %) and a tetragonal Ti_2Cu crystal structure (space group 139: I4/mmm) (Fig. 7C). For all compositions, some nano-scale spheroid particles of TiC were observed inside of the Ti-rich phases (Fig. 8A and 8B). These particles were likely present as an impurity in the Ti used to synthesize these alloys. No coherency or preferred orientation relationship between any of the second phases and the B19 matrix (Fig. 8C) were observed. For all alloy compositions with < 50 at. % Ti, the second phase with the largest volume fraction was $(Cu,Ni)_2Ti$ with a tetragonal crystal structure (space group 139: I4/mmm) (Fig. 8D).

In situ heating of the $Ni_{20}Ti_{50}Cu_{30}$ (at. %) alloy specimen to 120 °C was performed to characterize the NiTiCu in the B2 austenite phase (Fig. 7F). The lattice parameter of the B19 and B2 phases in this alloy were measured using selected area diffraction and found to be as a = 2.87 Å, b = 4.20 Å, c = 4.40 Å, and a_0 = 2.96 Å, respectively.

DSC results of the NiTiCu samples demonstrate clear martensitic transformation peaks (DSC for $Ni_xTi_{75-x}Cu_{25}$ shown in Fig. 9A) with excellent cyclic stability of transformation (Fig. 9B). After 80 heating-cooling cycles, the transformation peaks of $Ni_{29}Ti_{46}Cu_{25}$ and $Ni_{27}Ti_{48}Cu_{25}$ each shifted by only 0.04 °C and 0.50 °C, respectively (measured at the midpoint of the low-temperature slope of the austenite to martensite peak), and the alloys retained 100% of their first-cycle transformation enthalpies. The raw data from the 80-cycle DSC measurements is visualized using TA Universal Analysis software in Fig. 10. Fig. 10A demonstrates that there is very little temperature shift for $Ni_{29}Ti_{46}Cu_{25}$ with all cycles falling within a 0.04 °C temperature range. Fig. 10B shows a gradual temperature increase from the 1st cycle to the 80th cycle measured in $Ni_{27}Ti_{48}Cu_{25}$, with a 0.50 °C difference between the 1st and 80th cycles. It should be noted that the TA Q2000 DSC used to obtain these results has a temperature precision of ±0.01 °C, thus some portion of the temperature shift at such a fine measurement resolution could be attributed to random measurement error. The transformation temperatures A_f and M_f are plotted as a function of composition in Fig. 9C and Fig. 9D. An initial sharp decrease in transformation temperatures is observed upon decreasing Ti content below 50 at. %, followed by smooth descent in transformation temperatures with further decrease in Ti content. The OTRs of these alloys are plotted in Fig. 9E which shows a sharp increase in OTR occurring when Ni>35 at. %. The transformation temperatures for the third cycle from each composition can be found in Table 1. The latent heat of transformation values for the martensite to austenite transformation (presented in Table

1 and plotted in Fig. 11A) were calculated from the area under the DSC peaks and plotted against the area fraction of the second phase, as found using backscattered electron (BSE) images of the samples that can be seen as insets in Fig. 11.

Thermal conductivities of the alloys (Cu = 20, 22.5, 25 at. %) measured at approximately 100 °C in the austenite phase are plotted as a function of the second phase area fraction in Fig. 11B. In Fig. 13, the temperature dependent behavior of thermal conductivity and specific heat capacity in $Ni_{25}Ti_{50}Cu_{25}$ is shown. In addition to thermal conductivity and latent heat, the density of the material (Fig. 11C) was measured and used to calculate FOM (Fig. 11D). The calculated FOM, OTR, and A_f temperatures for the NiTiCu samples in this work is compared to traditional PCMs and other SMAs in Fig. 14. The FOM in combination with small OTR of the NiTiCu samples outperforms traditional PCMs and provides an alternative to NiTi and NiTiHf for small OTR with transformation temperatures slightly above room temperature.

4. Discussion of the Results

The NiTiCu system is known for excellent cyclic thermal stability of martensitic transformation [49-52], and the very small changes in the martensite and austenite peaks for each stress-free cycle in this work are among the smallest reported in NiTi-based SMAs. For comparison, Zarnetta et al. [53] demonstrated the cyclic stability of $Ni_{50}Ti_{50}$, $Ni_{35}Ti_{50}Cu_{15}$, and $Ni_{50}Ti_{39}Pd_{11}$, with the alloys showing transformation peak shifts after 20 thermal cycles of 12.5, 0.65, and 0.39 °C respectively (measured in the same manner as in this study). $Ni_{34.4}Ti_{50.2}Cu_{12.3}Pd_{3.1}$ showed greater cyclic stability than the other alloys from the study, with a temperature shift of 0.1 °C after 80 thermal cycles which was reported to be unprecedented at the time [53]. Bumke et al. [54] reported a ~0.1 °C temperature shift after 40 thermal cycles in a thin film of $Ti_{52.8}Ni_{22.2}Cu_{22.5}Co_{2.5}$ due to the improved crystallographic compatibility. Clearly, the transformation temperature shift with thermal cycling observed in the present study is the best reported to date in SMA literature.

The transformation peak shift with the number of thermal cycles is ascribed to the crystallographic compatibility between the austenite and martensite phases, described by λ_2 of the transformation stretch tensor and the strength of SMAs against dislocation plasticity [55]. Many of NiTiCu SMA compositions fabricated and tested in this study have λ_2 values close to 1, indicating superior compatibility between the transforming phases and thus negligible generation of lattice defects (dislocations) during martensitic transformation. For instance, based on the lattice parameters calculated from SADP, $Ni_{20}Ti_{50}Cu_{30}$ (at. %) has a λ_2 value of 1.003. This value is comparable to those reported for NiTiCu and NiTiPd alloys [56]. However, the correlation between λ_2 and thermal hysteresis / thermal stability is not sensitive enough to rationalize the small differences mentioned above.

In addition to the inherent lattice compatibility in NiTiCu alloys, another reason for the enhanced cyclic stability and small OTR could be the internal stresses at the interfaces between the transforming matrix and $(Cu,Ni)_2Ti$ precipitates, behaving similarly to Ti_2Cu precipitates in Ti-rich NiTiCu SMAs which enable the B2↔B19 transformation to follow the same low energy path during each thermal cycle and result in exceptional functional fatigue properties [45, 46]. However, this hypothesis is not valid as no coherency or preferred orientation relationship between $(Cu,Ni)_2Ti$ precipitates and the B19 matrix have been observed in TEM analyses. On the other hand, the coherent precipitates, despite their positive effect on reducing thermal hysteresis by suppressing inelastic accommodation of the transformation shear and volume change, lead to an increase in OTR by enhancing the elastic energy storage during transformation [24]. Furthermore, second phases in Ti-lean NiTiCu compositions increased in size up to tens of micrometers with increasing Ni content as shown in the inset of Fig. 11. While no hardening effect of the matrix could be expected due to the incoherency of these large second phases, the effective grain size of the transforming matrix decreases

with increasing area fraction of second phases. Typically, a reduction in grain size of SMAs is accompanied by a reduction of the martensite plate size and an increase in thermal hysteresis as shown in Cu-based SMAs [57]. Although OTR and thermal hysteresis values of Ti-lean NiTiCu SMAs of the current study (e.g., $Ni_xTi_{75-x}Cu_{25}$) increased with increasing Ni content (and area fraction of second phases), thermal stability of the SMAs would be expected to decrease. However, this contradicts our results where $Ni_{29}Ti_{46}Cu_{25}$ exhibits a much better thermal stability compared to $Ni_{27}Ti_{48}Cu_{25}$ (Fig. 9B). Therefore, in the present case, it is likely that $(Cu,Ni)_2Ti$ precipitates help accommodate the transformation shear and small volume change of the matrix phase during the transformation, minimize the defect storage in the matrix during the forward and reverse transformation in the matrix, and combined with the inherent superior lattice compatibility between austenite and martensite phase in the matrix, lead to the observed ultra-low transformation temperature shift upon thermal cycling. However, the exact underlying mechanisms responsible for such stability is not very clear, and requires further study. Regardless, the NiTiCu SMAs shown in Fig. 9 present great potential for SMA applications requiring a high degree of cyclic thermal stability of martensitic transformation with a small OTR.

The slower cooling rate during air cooling than that during water quenching after homogenization likely contributed to the small OTR in the NiTiCu samples. It has been shown in both NiTi-based [58] and Cu-based [59] SMAs that thermal hysteresis is dependent on quench media, with rapid cooling rates yielding an increase in defect generation and thermal hysteresis, and thus OTR. In a high-throughput study on thin film NiTiCu alloys, Zarnetta et al. [38] reported that thermal hysteresis had a negative correlation with annealing temperature, with the smallest resulting OTR in the $Ti_{50}Ni_{50-x}Cu_x$ stoichiometric compositions at an annealing temperature of 700 ˚C. They reported that the coarsening of precipitate phases such as Ti-rich and (Ni, Cu)-rich phases were responsible for the observed decrease in thermal hysteresis. Coarsening of the precipitate phases was usually associated with a loss of coherency and a decrease of the precipitate strengthening effect on the matrix, facilitating the martensite propagation (similar to what is observed in the present study). However, they only reported heat treatments of up to 700 ˚C for 1 h. The high temperature homogenization treatment used in this study (925 ˚C) as well as longer treatment time (48 h) likely resulted in coarser precipitates, reducing the amount of stored elastic energy due to the precipitates upon martensitic transformation and contributing to the small OTRs observed.

The latent heat of transformation has a decreasing linear relationship with the area fraction of the second phase (brighter regions in the inset figures) in the materials (Fig. 11A). This is, in part, because the second phase replaces a portion of the transforming material, resulting in a lower amount of transforming material within a bulk sample, and therefore a lower overall latent heat is measured in the sample. However, the percentage decrease in latent heat is of greater magnitude than expected based on the decrease in the mass

fraction of transforming material alone, indicating that there is another contributing factor. The latent heat of transformation can be normalized by the mass fraction of the transforming phase to determine the true transformation enthalpy of the transforming phase. Using the trends in measured density for the alloys from Fig. 11C, the densities can be approximated for the transforming matrix (ρ_m = 6333 kg/m^3) and for the second phase (ρ_{sp} = 7611 kg/m^3). Next, using the area fraction of the second phase (A_{sp}), the mass fraction of the transforming matrix, M_m, can be approximated using Eq. (1):

$$M_m = 1 - \frac{(A_{sp} * \rho_{sp})}{(A_{sp} * \rho_{sp}) + ((1 - A_{sp}) * \rho_m)} \qquad \text{Eq. (1)}$$

The calculated M_m is then used to normalize the latent heat of transformation using Eq. (2)

$$\Delta H_{norm} = \frac{\Delta H_{M-A}}{M_m} \qquad \text{Eq. (2)}$$

The normalized latent heat versus the second phase area fraction is shown in Fig. 12A. The results indicate that some other mechanism besides the changing volume fraction of transforming material affects the transformation enthalpy, as the normalized latent heat is still dependent on the amount of second phase. It is possible that different amounts of the second phase could influence the martensite variant evolution, and thus entropy and transformation enthalpy, nanoparticles could be present in the transforming phase, although none were observed in TEM, or some other second phase formation related effect could be occurring. The effect of Ni content (as confirmed by EDX) on the enthalpy was also explored (Fig. 12B) revealing decreasing trends with Ni content for various nominal Cu contents, but the separation between the different nominal Cu contents suggests the variation in enthalpy is independent of composition. After normalizing the latent heat by the mass fraction of transforming material, there remains a decreasing trend in latent heat versus the second phase area fraction (Fig. 12A) with no correlation to the transforming matrix composition (Fig. 12B). The remaining trend in normalized latent heat with respect to the second phase area fraction may be an effect of the confinement of martensitic domains by the second phase, reducing the number and size of martensitic variant formation.

Between 0 and 15% second phase, thermal conductivity remains relatively constant between 7.7 and 10.5 Wm^{-1}K^{-1} (Fig. 11B). As the second phase area fraction increases further, thermal conductivity follows an upward trend, reaching a maximum value of 16.5 Wm^{-1}K^{-1} at just over 50% second phase. This increasing trend indicates that the thermal conductivity of the second phase is higher than that of the austenite phase, contributing to a higher effective thermal conductivity as measured in the bulk material. The nearly constant thermal conductivity measured in the bulk material between 0 and 15% second phase may be attributed to competing factors which negate the effects of one another. The thermal conductivity is positively affected by the addition of a more conductive second phase but negatively affected by phonon scattering at the phase

boundaries [60]. Note that 30 at. % Cu samples were not large enough to obtain thermal diffusivity samples, and thus, it was not possible to obtain their thermal conductivity values. In addition, the trend in thermal conductivity with respect to the second phase is already well established with the samples of three other Cu contents, it was not necessary to fabricate more 30 at. % Cu samples to establish the same trend. The specific heat capacities of the alloys in the austenite phase were measured to be between 0.33 and 0.50 $Jg^{-1}K^{-1}$, however no correlation was found with respect to alloy composition or second phase area fraction.

Beginning at -75 °C in the martensite phase, thermal conductivity increased with temperature up to the start of the transformation region (Fig. 13). After transformation to the austenite phase, thermal conductivity continued to increase with rising temperature at a similar rate as in the martensite phase. Specific heat capacity increased gradually between -75 °C and the transformation region, spiked sharply during transformation, and decreased below the martensite specific heat capacity level upon completing transformation to austenite. The large spike in measured specific heat capacity observed within the transformation region is a result of the latent heat of transformation, and therefore cannot be attributed to sensible heating. The behaviors of thermal conductivity and specific heat capacity observed in this work are similar to those measured in $Ni_{50}Ti_{40}Cu_{10}$ by Ingale et al. [61]. Because all the studied NiTiCu alloys showed similar temperature dependent thermophysical property behavior, the trends shown for $Ni_{25}Ti_{50}Cu_{25}$ in Fig. 13 are representative of the other alloys.

As with transformation enthalpy and thermal conductivity, the densities of the alloys showed a strong correlation with second phase area fraction as shown in Fig. 11C. Density was found to increase linearly from below 6400 kg/m^3 at 0% second phase to over 7100 kg/m^3 at 50% second phase. Taking the product of the transformation enthalpy (Fig. 11A), thermal conductivity (Fig. 11B), and density (Fig. 11C), the FOM of the alloys is obtained as a function of the second phase area fraction as shown in Fig. 11D. Despite density and thermal conductivity both showing positive correlations with the second phase area fraction, the FOM decreases with increasing second phase area fraction, indicating that FOM is dominated by the decreasing trend in transformation enthalpy. The reason for this is apparent when considering that the highest transformation enthalpy value is 6 times the lowest value, however thermal conductivity and density only vary by a factor of 2 and 1.2, respectively. From the trend shown in Fig. 11D, it is apparent that PCM performance in NiTiCu SMAs as quantified by FOM can be optimized by selecting compositions near 50% Ti, containing no second phase. For applications in which high thermal conductivity is most important, thermal conductivity can be increased to desired levels by increasing second phase volume fraction, however this is done at the cost of decreasing transformation enthalpy and overall FOM.

In Fig. 14, FOM is plotted against OTR for the NiTiCu SMAs studied here, with data from traditional polymer-based solid-to-solid PCMs [62-64], composite PCMs [15-18], and NiTi [1] and NiTiHf [3] SMAs

included for comparison. The A_F temperature of each material (equivalently, the melting peak endpoint temperature for traditional PCMs) is denoted by marker color. As shown in Fig. 14, NiTi and NiTiHf SMAs have FOM values much higher than traditional PCMs. However, these SMAs generally have higher OTRs, limiting their application and giving them lower thermal cycling frequency. The magnified portion of Fig. 14 shows that NiTiCu SMAs achieve higher FOM than traditional PCMs while exhibiting OTRs much lower than NiTi and NiTiHf SMAs, with most NiTiCu alloys showing OTRs between 12 and 20 °C. Although polymer-based solid-to-solid PCMs show similarly low OTRs, they have extremely low FOM values ranging from 3 to 26 $10^6 \cdot J^2/K \cdot s \cdot m^4$ compared to NiTiCu SMAs which range between FOM values of 250 and 1050 $10^6 \cdot J^2/K \cdot s \cdot m^4$. This unique combination of high FOM and low OTR in NiTiCu alloys makes them excellent candidates for thermal energy storage and management applications where high heat flux, fast thermal cycling, and/or a narrow operation temperature window are required.

5. Summary and Conclusions

A promising composition region of the NiTiCu shape memory alloy system with narrow OTR was explored to identify candidate alloys for thermal energy storage and management, and the transformation characteristics and thermophysical properties of the alloys therein were examined. The NiTiCu alloys studied here present many characteristics which make them attractive candidates for use as PCMs for thermal energy storage and management applications. Their unique combination of high FOM ranging from 250 to 1050 $10^6 \cdot J^2/K \cdot s \cdot m^4$, and small overall transformation range (OTR, A_f-M_f) with most alloys ranging between 12 and 20 °C, indicates that they can have excellent performance in high-power TES and management applications and the ability to undergo frequent thermal cycling within narrow temperature ranges. Additionally, the alloys exhibit superior cyclic stability, showing only 0.04 °C to 0.51 °C shift in the transformation peak and no degradation in transformation enthalpy after 80 thermal cycles, one of the best among all SMAs studied to date. The trends in transformation temperatures with respect to composition allow for tuning of NiTiCu alloys for specific TES applications through composition control, with A_F temperatures ranging from -8.1 °C to 88.7°C. Furthermore, the differences in material properties between the primary and second phases present an opportunity to tailor the properties of the material (e.g., thermal conductivity) to desired levels by adjusting the ratio of the two phases. Thus, SMAs are further established as potential high performance PCMs, with NiTiCu SMAs providing unique, tunable TES solutions, having low OTRs while maintaining high FOM values.

Acknowledgments

The authors at Texas A&M University acknowledge the financial support from the National Science Foundation, under Grant No. 2,119,103 (DMREF: AI-Guided Accelerated Discovery of Multi-Principal Element Multi-Functional Alloys), Army Research Laboratory under the Cooperative Agreement W911NF-19-2-0264, and the Data-Enabled Discovery and Design of Energy Materials (D^3EM) program funded through NSF-NRT Award DGE-1545403.

Data availability:

The data supporting the findings in this study are available within the paper and corresponding references. Any further information or clarification is available from the corresponding author upon reasonable request.

Author Contributions

W.T., N.H., D.J.S., and I.K. were responsible for the study design. W.T. and R.O. synthesized and processed the alloys. R.S., A.C.L. and R.O. imaged the alloys. N.H., D.J.S., A.A.W, and A.C.L. were responsible for specific heat, diffusivity, and density measurements. W.T., N.H., R.O., R.S. and K.C.A. made substantial contributions to the acquisition, analysis, or interpretation of data for the work. W.T., N.H., R.S., K.C.A. and I.K. drafted the work or revised it critically for important intellectual content. All authors read and approved the final manuscript.

Competing Interests: The authors declare no competing interests.

References

1. Sharar, D.J., B.F. Donovan, R.J. Warzoha, A.A. Wilson, A.C. Leff, and B.M. Hanrahan, *Solid-state thermal energy storage using reversible martensitic transformations.* Applied Physics Letters, 2019. **114**(14).

2. Sharar, D.J., A.C. Leff, A.A. Wilson, and A. Smith, *High-capacity high-power thermal energy storage using solid-solid martensitic transformations.* Applied Thermal Engineering, 2021. **187**: p. 116490.

3. Hite, N., D.J. Sharar, W. Trehern, T. Umale, K.C. Atli, A.A. Wilson, A.C. Leff, and I. Karaman, *NiTiHf shape memory alloys as phase change thermal storage materials.* Acta Materialia, 2021. **218**: p. 117175.

4. Irfan Lone, M. and R. Jilte, *A review on phase change materials for different applications.* Materials Today: Proceedings, 2021.

5. De Gracia, A. and L.F. Cabeza, *Phase change materials and thermal energy storage for buildings.* Energy and Buildings, 2015. **103**: p. 414-419.

6. Kuznik, F., D. David, K. Johannes, and J.-J. Roux, *A review on phase change materials integrated in building walls.* Renewable and Sustainable Energy Reviews, 2011. **15**(1): p. 379-391.

7. Mondal, S., *Phase change materials for smart textiles–An overview.* Applied thermal engineering, 2008. **28**(11-12): p. 1536-1550.

8. Jankowski, N.R. and F.P. McCluskey, *A review of phase change materials for vehicle component thermal buffering.* Applied energy, 2014. **113**: p. 1525-1561.

9. Limited, P.C.M.P. *PlusICE Phase Change Materials*. 2013; Available from: https://www.pcmproducts.net/files/PlusICE%20Range-2013.pdf.

10. Hite, N., D. Sharar, W. Trehern, T. Umale, K. Atli, A. Wilson, A. Leff, and I. Karaman, *NiTiHf shape memory alloys as phase change thermal storage materials.* Acta Materialia, 2021. **218**: p. 117175.

11. Sharar, D.J., B.F. Donovan, R.J. Warzoha, A.A. Wilson, A.C. Leff, and B.M. Hanrahan, *Solid-state thermal energy storage using reversible martensitic transformations.* Applied Physics Letters, 2019. **114**(14): p. 143902.

12. Lu, T.J., *Thermal management of high power electronics with phase change cooling.* International Journal of Heat and Mass Transfer, 2000. **43**(13): p. 2245-2256.

13. Shamberger, P.J., *Cooling Capacity Figure of Merit for Phase Change Materials.* Journal of Heat Transfer, 2015. **138**(2).

14. Shao, L., A. Raghavan, G.-H. Kim, L. Emurian, J. Rosen, M.C. Papaefthymiou, T.F. Wenisch, M.M.K. Martin, and K.P. Pipe, *Figure-of-merit for phase-change materials used in thermal management.* International Journal of Heat and Mass Transfer, 2016. **101**: p. 764-771.

15. Wu, X., M. Gao, K. Wang, Q. Wang, C. Cheng, Y. Zhu, F. Zhang, and Q. Zhang, *Experimental Study of the Thermal Properties of a Homogeneous Dispersion System of a Paraffin-based Composite Phase Change Materials.* Journal of Energy Storage, 2021. **36**: p. 102398.

16. Wu, B., D. Lao, R. Fu, X. Su, H. Liu, and X. Jin, *Novel PEG/EP form-stable phase change materials with high thermal conductivity enhanced by 3D ceramics network.* Ceramics International, 2020. **46**(16, Part A): p. 25285-25292.

17. Li, M., *A nano-graphite/paraffin phase change material with high thermal conductivity.* Applied Energy, 2013. **106**: p. 25-30.

18. Zeng, J.-L., J. Gan, F.-R. Zhu, S.-B. Yu, Z.-L. Xiao, W.-P. Yan, L. Zhu, Z.-Q. Liu, L.-X. Sun, and Z. Cao, *Tetradecanol/expanded graphite composite form-stable phase change material for thermal energy storage.* Solar Energy Materials and Solar Cells, 2014. **127**: p. 122-128.

19. Frenzel, J., E.P. George, A. Dlouhy, C. Somsen, M.-X. Wagner, and G. Eggeler, *Influence of Ni on martensitic phase transformations in NiTi shape memory alloys.* Acta Materialia, 2010. **58**(9): p. 3444-3458.

20. Payne, S.A., R.J. Beach, C. Bibeau, C.A. Ebbers, M.A. Emanuel, E.C. Honea, C.D. Marshall, R.H. Page, K.I. Schaffers, and J.A. Skidmore, *Diode arrays, crystals, and thermal management for solid-state lasers.* IEEE Journal of Selected Topics in Quantum Electronics, 1997. **3**(1): p. 71-81.

21. Sato, Y., N. Yoshida, Y. Tanabe, H. Fujita, and N. Ooiwa, *Characteristics of a new power generation system with application of a Shape Memory Alloy Engine.* Electrical Engineering in Japan, 2008. **165**(3): p. 8-15.

22. Wang, Z., X. Zu, S. Zhu, and L. Wang, *Temperature memory effect induced by incomplete transformation in TiNi shape memory alloy.* Materials Letters, 2005. **59**(4): p. 491-494.

23. Liu, Y., J. Laeng, T. Chin, and T.-H. Nam, *Effect of incomplete thermal cycling on the transformation behaviour of NiTi.* Materials Science and Engineering: A, 2006. **435**: p. 251-257.

24. Hamilton, R.F., H. Sehitoglu, Y. Chumlyakov, and H.J. Maier, *Stress dependence of the hysteresis in single crystal NiTi alloys.* Acta Materialia, 2004. **52**(11): p. 3383-3402.

25. Zhang, Z., R.D. James, and S. Müller, *Energy barriers and hysteresis in martensitic phase transformations.* Acta Materialia, 2009. **57**(15): p. 4332-4352.

26. Ball, J.M., C. Chu, and R.D. James, *Hysteresis during stress-induced variant rearrangement.* Le Journal de Physique IV, 1995. **5**(C8): p. C8-245-C8-251.

27. Atli, K., B. Franco, I. Karaman, D. Gaydosh, and R. Noebe, *Influence of crystallographic compatibility on residual strain of TiNi based shape memory alloys during thermo-mechanical cycling.* Materials Science and Engineering: A, 2013. **574**: p. 9-16.

28. Potapov, P., A. Shelyakov, A. Gulyaev, E. Svistunov, N. Matveeva, and D. Hodgson, *Effect of Hf on the structure of Ni-Ti martensitic alloys.* Materials Letters, 1997. **32**(4): p. 247-250.

29. Evirgen, A., I. Karaman, R. Santamarta, J. Pons, C. Hayrettin, and R. Noebe, *Relationship between crystallographic compatibility and thermal hysteresis in Ni-rich NiTiHf and NiTiZr high temperature shape memory alloys.* Acta Materialia, 2016. **121**: p. 374-383.

30. Cui, J., Y.S. Chu, O.O. Famodu, Y. Furuya, J. Hattrick-Simpers, R.D. James, A. Ludwig, S. Thienhaus, M. Wuttig, and Z. Zhang, *Combinatorial search of thermoelastic shape-memory alloys with extremely small hysteresis width.* Nature materials, 2006. **5**(4): p. 286-290.

31. Evirgen, A., F. Basner, I. Karaman, R.D. Noebe, J. Pons, and R. Santamarta, *Effect of aging on the martensitic transformation characteristics of a Ni-rich NiTiHf high temperature shape memory alloy.* Functional Materials Letters, 2012. **5**(04): p. 1250038.

32. Frenzel, J., A. Wieczorek, I. Opahle, B. Maaß, R. Drautz, and G. Eggeler, *On the effect of alloy composition on martensite start temperatures and latent heats in Ni–Ti-based shape memory alloys.* Acta Materialia, 2015. **90**: p. 213-231.

33. James, R.D. and K.F. Hane, *Martensitic transformations and shape-memory materials.* Acta materialia, 2000. **48**(1): p. 197-222.

34. Zarinejad, M. and Y. Liu, *Dependence of Transformation Temperatures of NiTi-based Shape-Memory Alloys on the Number and Concentration of Valence Electrons.* Advanced Functional Materials, 2008. **18**(18): p. 2789-2794.

35. Nespoli, A., E. Villa, and S. Besseghini, *Characterization of the martensitic transformation in Ni50−xTi50Cux alloys through pure thermal measurements.* Journal of alloys and compounds, 2011. **509**(3): p. 644-647.

36. Zhang, Z., J. Frenzel, K. Neuking, and G. Eggeler, *Vacuum induction melting of ternary NiTiX (X= Cu, Fe, Hf, Zr) shape memory alloys using graphite crucibles.* Materials transactions, 2006. **47**(3): p. 661-669.

37. Sehitoglu, H., I. Karaman, X. Zhang, A. Viswanath, Y. Chumlyakov, and H.J. Maier, *Strain–temperature behavior of NiTiCu shape memory single crystals.* Acta Materialia, 2001. **49**(17): p. 3621-3634.

38. Zarnetta, R., P.J.S. Buenconsejo, A. Savan, S. Thienhaus, and A. Ludwig, *High-throughput study of martensitic transformations in the complete Ti–Ni–Cu system.* Intermetallics, 2012. **26**: p. 98-109.

39. Hattori, Y., T. Taguchi, H.Y. Kim, and S. Miyazaki, *Effect of stoichiometry on shape memory properties and functional stability of Ti–Ni–Pd alloys.* Materials, 2019. **12**(5): p. 798.

40. Atli, K., I. Karaman, and R. Noebe, *Work output of the two-way shape memory effect in Ti50. 5Ni24. 5Pd25 high-temperature shape memory alloy.* Scripta Materialia, 2011. **65**(10): p. 903-906.

41. Nam, T.H., T. Saburi, and K.i. Shimizu, *Cu-content dependence of shape memory characteristics in Ti–Ni–Cu alloys.* Materials Transactions, JIM, 1990. **31**(11): p. 959-967.

42. Li, H., K. Qiu, F. Zhou, L. Li, and Y. Zheng, *Design and development of novel antibacterial Ti-Ni-Cu shape memory alloys for biomedical application.* Scientific reports, 2016. **6**(1): p. 1-11.

43. International, A., *Standard Test Method for Transformation Temperature of Nickel-Titanium Alloys by Thermal Analysis*. 2017.

44. Zhu, W.J., L.I. Duarte, and C. Leinenbach, *Experimental study and thermodynamic assessment of the Cu–Ni–Ti system.* Calphad, 2014. **47**: p. 9-22.

45. Chluba, C., W. Ge, R.L. de Miranda, J. Strobel, L. Kienle, E. Quandt, and M. Wuttig, *Ultralow-fatigue shape memory alloy films.* Science, 2015. **348**(6238): p. 1004-1007.

46. Gu, H., L. Bumke, C. Chluba, E. Quandt, and R.D. James, *Phase engineering and supercompatibility of shape memory alloys.* Materials Today, 2018. **21**(3): p. 265-277.

47. Trehern, W., R. Ortiz-Ayala, K.C. Atli, R. Arroyave, and I. Karaman, *Data-driven shape memory alloy discovery using Artificial Intelligence Materials Selection (AIMS) framework.* Acta Materialia, 2022. **228**: p. 117751.

48. Nam, T.H., T. Saburi, Y. Nakata, and K.i. Shimizu, *Shape memory characteristics and lattice deformation in Ti–Ni–Cu alloys.* Materials Transactions, JIM, 1990. **31**(12): p. 1050-1056.

49. He, X.-m., L.-z. Zhao, X.-m. Wang, R.-f. Zhang, and M.-s. Li, *Transformation behaviour with thermal cycling in Ti50Ni43Cu7 shape memory alloy.* Materials Science and Engineering: A, 2006. **427**(1-2): p. 327-330.

50. Nam, T., G. Ha, H. Lee, and S. Hur, *Effect of thermal cycling on martensitic transformation temperatures in Ti–Ni–Cu shape memory alloys.* Materials science and technology, 2000. **16**(9): p. 1017-1021.

51. Jean, R.-D. and J.-B. Duh, *The thermal cycling effect on Ti-Ni-Cu shape memory alloy.* Scripta metallurgica et materialia, 1995. **32**(6).

52. Rong, L., D.A. Miller, and D.C. Lagoudas, *Transformation behavior in a thermomechanically cycled TiNiCu alloy.* Metallurgical and materials transactions A, 2001. **32**(11): p. 2689-2693.

53. Zarnetta, R., R. Takahashi, M.L. Young, A. Savan, Y. Furuya, S. Thienhaus, B. Maaß, M. Rahim, J. Frenzel, and H. Brunken, *Identification of quaternary shape memory alloys with near-zero thermal hysteresis and unprecedented functional stability.* Advanced Functional Materials, 2010. **20**(12): p. 1917-1923.

54. Bumke, L., C. Zamponi, J. Jetter, and E. Quandt, *Cu-rich Ti52. 8Ni22. 2Cu22. 5Co2. 5 shape memory alloy films with ultra-low fatigue for elastocaloric applications.* Journal of Applied Physics, 2020. **127**(22): p. 225105.

55. Moshref-Javadi, M., S.H. Seyedein, M.T. Salehi, and M.R. Aboutalebi, *Age-induced multi-stage transformation in a Ni-rich NiTiHf alloy.* Acta materialia, 2013. **61**(7): p. 2583-2594.

56. Delville, R., D. Schryvers, Z. Zhang, and R.D. James, *Transmission electron microscopy investigation of microstructures in low-hysteresis alloys with special lattice parameters.* Scripta Materialia, 2009. **60**(5): p. 293-296.

57. Roca, P.L., L. Isola, P. Vermaut, and J. Malarría, *Relationship between grain size and thermal hysteresis of martensitic transformations in Cu-based shape memory alloys.* Scripta Materialia, 2017. **135**: p. 5-9.

58. Acar, E., S. Saedi, G.P. Toker, H. Tobe, and H.E. Karaca, *Post-aging cooling rate effects in Ni45.3Ti34.7Hf15Pd5 shape memory alloys.* Materials Research Bulletin, 2021. **133**: p. 111016.

59. Canbay, C.A., O. Karaduman, N. Ünlü, S.A. Baiz, and İ. Özkul, *Heat treatment and quenching media effects on the thermodynamical, thermoelastical and structural characteristics of a new Cu-based quaternary shape memory alloy.* Composites Part B: Engineering, 2019. **174**: p. 106940.

60. Carrete, J., M. López-Suárez, M. Raya-Moreno, A.S. Bochkarev, M. Royo, G.K.H. Madsen, X. Cartoixà, N. Mingo, and R. Rurali, *Phonon transport across crystal-phase interfaces and twin boundaries in semiconducting nanowires.* Nanoscale, 2019. **11**(34): p. 16007-16016.

61. Ingale, B., W. Wei, P. Chang, Y. Kuo, and S.-K. Wu, *Anomalous transport and thermal properties of NiTi and with Cu and Fe-doped shape memory alloys near the martensitic transition.* Journal of Applied Physics, 2011. **110**: p. 113721.

62. Sarı, A., C. Alkan, A. Biçer, and A. Karaipekli, *Synthesis and thermal energy storage characteristics of polystyrene-graft-palmitic acid copolymers as solid–solid phase change materials.* Solar Energy Materials and Solar Cells, 2011. **95**(12): p. 3195-3201.

63. Sarı, A., C. Alkan, and Ö. Lafçı, *Synthesis and thermal properties of poly(styrene-co-ally alcohol)-graft-stearic acid copolymers as novel solid–solid PCMs for thermal energy storage.* Solar Energy, 2012. **86**(9): p. 2282-2292.

64. Sarı, A., C. Alkan, and A. Biçer, *Synthesis and thermal properties of polystyrene-graft-PEG copolymers as new kinds of solid–solid phase change materials for thermal energy storage.* Materials Chemistry and Physics, 2012. **133**(1): p. 87-94.

65. Chang, S.-H. and S.-H. Hsiao, *Inherent internal friction of Ti50Ni50− xCux shape memory alloys measured under isothermal conditions.* Journal of alloys and compounds, 2014. **586**: p. 69-73.

66. Nam, T.H., T. Saburi, and K.i. Shimizu, *Effect of thermo-mechanical treatment on shape memory characteristics in a Ti-40Ni-10Cu (at%) alloy.* Materials Transactions, JIM, 1991. **32**(9): p. 814-820.

67. Lin, K. and S. Wu, *Annealing effect on martensitic transformation of severely cold-rolled Ti50Ni40Cu10 shape memory alloy.* Scripta materialia, 2007. **56**(7): p. 589-592.

68. Bertacchini, O.W., D.C. Lagoudas, and E. Patoor, *Thermomechanical transformation fatigue of tinicu sma actuators under a corrosive environment–part i: Experimental results.* International Journal of Fatigue, 2009. **31**(10): p. 1571-1578.

69. Besseghini, S., E. Villa, and A. Tuissi, *Ni□ Ti□ Hf shape memory alloy: effect of aging and thermal cycling.* Materials Science and Engineering: A, 1999. **273**: p. 390-394.

70. Chastaing, K., P. Vermaut, P. Ochin, C. Segui, J. Laval, and R. Portier, *Effect of Cu and Hf additions on NiTi martensitic transformation.* Materials Science and Engineering: A, 2006. **438**: p. 661-665.

71. Dai Hsu, D.H., B.C. Hornbuckle, B. Valderrama, F. Barrie, H.B. Henderson, G.B. Thompson, and M.V. Manuel, *The effect of aluminum additions on the thermal, microstructural, and mechanical behavior of NiTiHf shape memory alloys.* Journal of Alloys and Compounds, 2015. **638**: p. 67-76.

72. Ded, G.S., *Characterization of Ni-rich NiTiHf based high temperature shape memory alloys.* 2010.

73. Evirgen, A., I. Karaman, R. Santamarta, J. Pons, and R. Noebe, *Microstructural characterization and shape memory characteristics of the Ni50. 3Ti34. 7Hf15 shape memory alloy.* Acta Materialia, 2015. **83**: p. 48-60.

74. Evirgen, A., I. Karaman, R. Noebe, R. Santamarta, and J. Pons, *Effect of precipitation on the microstructure and the shape memory response of the Ni50. 3Ti29. 7Zr20 high temperature shape memory alloy.* Scripta Materialia, 2013. **69**(5): p. 354-357.

75. Evirgen, A., I. Karaman, J. Pons, R. Santamarta, and R. Noebe, *Role of nano-precipitation on the microstructure and shape memory characteristics of a new Ni50. 3Ti34. 7Zr15 shape memory alloy.* Materials Science and Engineering: A, 2016. **655**: p. 193-203.

76. Golberg, D., Y. Xu, Y. Murakami, S. Morito, K. Otsuka, T. Ueki, and H. Horikawa, *Characteristics of Ti50Pd30Ni20 high-temperature shape memory alloy.* Intermetallics, 1995. **3**(1): p. 35-46.

77. Grossmann, C., J. Frenzel, V. Sampath, T. Depka, and G. Eggeler, *Elementary transformation and deformation processes and the cyclic stability of NiTi and NiTiCu shape memory spring actuators.* Metallurgical and Materials Transactions A, 2009. **40**(11): p. 2530-2544.

78. Grossmann, C., J. Frenzel, V. Sampath, T. Depka, A. Oppenkowski, C. Somsen, K. Neuking, W. Theisen, and G. Eggeler, *Processing and property assessment of NiTi and NiTiCu shape memory actuator springs.* Materialwissenschaft Und Werkstofftechnik: Entwicklung, Fertigung, Prüfung, Eigenschaften Und Anwendungen Technischer Werkstoffe, 2008. **39**(8): p. 499-510.

79. Khan, M.I., H.Y. Kim, Y. Namigata, T.-h. Nam, and S. Miyazaki, *Combined effects of work hardening and precipitation strengthening on the cyclic stability of TiNiPdCu-based high-temperature shape memory alloys.* Acta materialia, 2013. **61**(13): p. 4797-4810.

80. Khan, M.I., H.Y. Kim, T.-h. Nam, and S. Miyazaki, *Formation of nanoscaled precipitates and their effects on the high-temperature shape-memory characteristics of a Ti50Ni15Pd25Cu10 alloy.* Acta materialia, 2012. **60**(16): p. 5900-5913.

81. Kim, K.M., J.K. Hong, C.H. Park, and J.-T. Yeom, *Comparative Study of the Thermocyclic Behavior of Ti–Ni–Hf and Ti–Ni–Hf–Ta Shape Memory Alloys.* Journal of Nanoscience and Nanotechnology, 2016. **16**(11): p. 11775-11778.

82. Lin, B., K. Gall, H.J. Maier, and R. Waldron, *Structure and thermomechanical behavior of NiTiPt shape memory alloy wires.* Acta biomaterialia, 2009. **5**(1): p. 257-267.

83. Umale, T., D. Salas, B. Tomes, R. Arroyave, and I. Karaman, *The effects of wide range of compositional changes on the martensitic transformation characteristics of NiTiHf shape memory alloys.* Scripta Materialia, 2019. **161**: p. 78-83.

84. Hsieh, S. and S. Wu, *A study on ternary Ti-rich TiNiZr shape memory alloys.* Materials characterization, 1998. **41**(4): p. 151-162.

85. Sasaki, T.T., B.C. Hornbuckle, R.D. Noebe, G.S. Bigelow, M.L. Weaver, and G.B. Thompson, *Effect of aging on microstructure and shape memory properties of a Ni-48Ti-25Pd (At. Pct) alloy.* Metallurgical and Materials Transactions A, 2013. **44**(3): p. 1388-1400.

86. Ramaiah, K., C. Saikrishna, and S. Bhaumik, *Ni24. 7Ti50. 3Pd25. 0 high temperature shape memory alloy with narrow thermal hysteresis and high thermal stability.* Materials & Design (1980-2015), 2014. **56**: p. 78-83.

87. Meng, X.L., Y.D. Fu, W. Cai, J. Zhang, Q.F. Li, and L.C. Zhao. *Martensitic Transformation Behavior and Shape Memory Effect of an Aged Ni-rich Ti-Ni-Hf High Temperature Shape Memory Alloy*. in *Solid State Phenomena*. 2008. Trans Tech Publ.

88. Patriarca, L. and H. Sehitoglu, *High-temperature superelasticity of Ni50. 6Ti24. 4Hf25. 0 shape memory alloy.* Scripta Materialia, 2015. **101**: p. 12-15.

89. Hornbuckle, B., T. Sasaki, G. Bigelow, R. Noebe, M. Weaver, and G. Thompson, *Structure–property relationships in a precipitation strengthened Ni–29.7 Ti–20Hf (at%) shape memory alloy.* Materials Science and Engineering: A, 2015. **637**: p. 63-69.

LIST of FIGURES

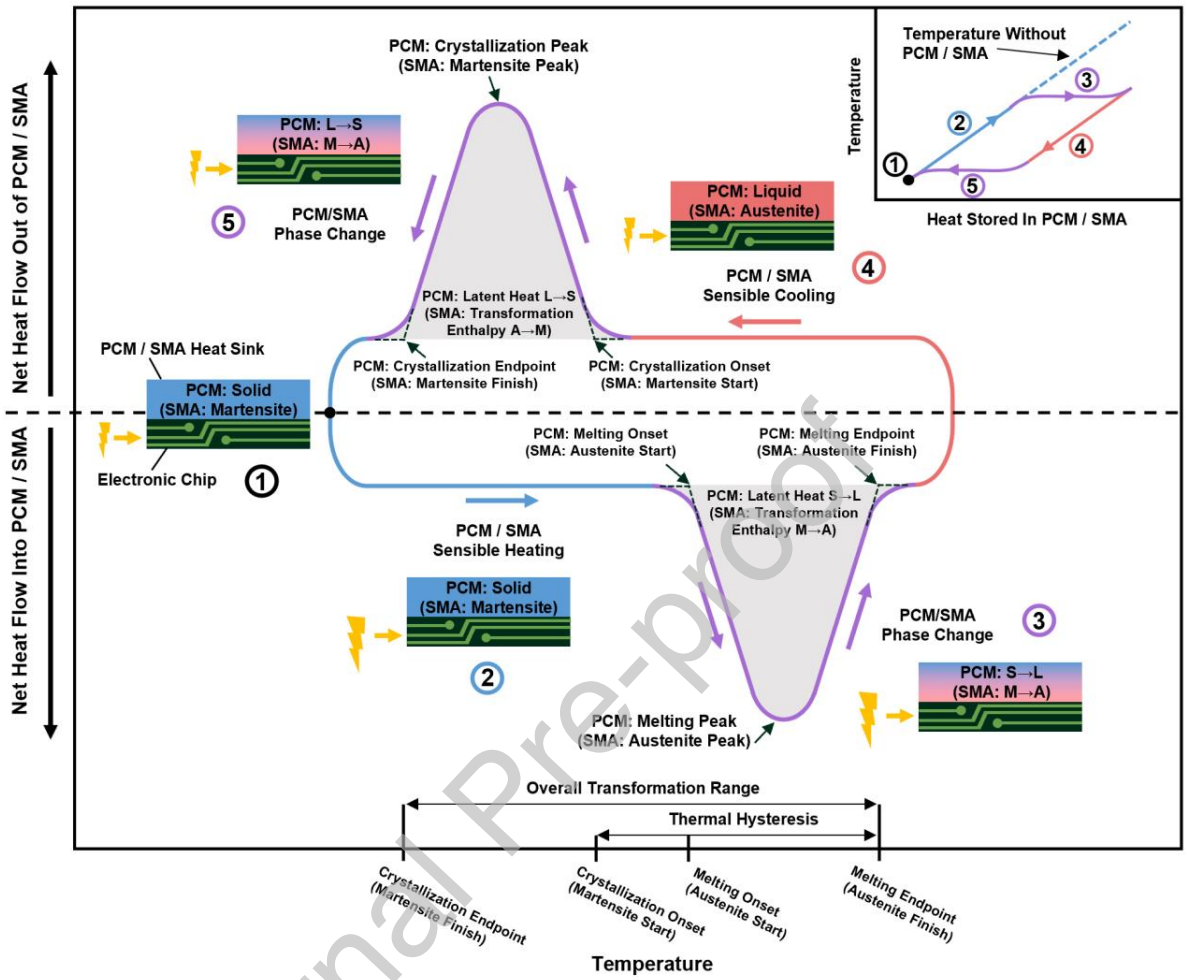

Fig. 1. Representative heat flow vs. temperature curve, shown as if measured by differential scanning calorimetry (DSC), illustrating typical behavior of Phase Change Materials (PCMs) undergoing melting and recrystallization, or equivalently, Shape Memory Alloys (SMAs) undergoing reverse and forward martensitic transformation in a thermal management application. PCM transformation temperatures are labeled with typical nomenclature, and equivalent corresponding transformation temperatures of SMAs are labeled in parenthesis. The effect of thermal management via PCM/SMA implementation on system temperature is represented in the inset at top-right.

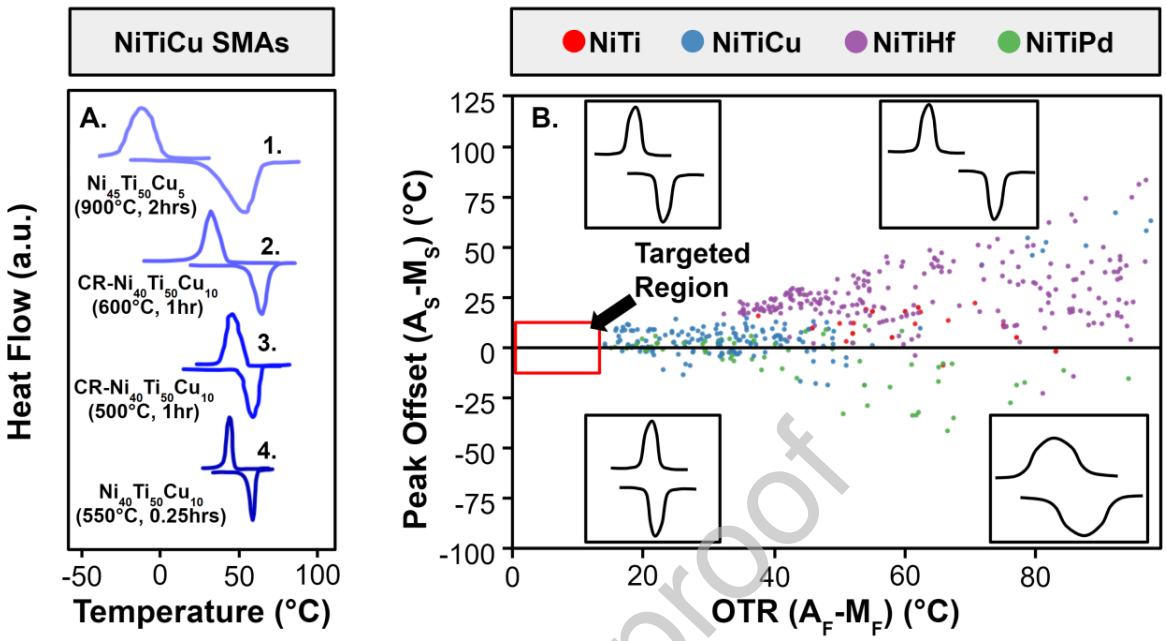

Fig. 2. (A) Adapted DSC plots from literature for solution heat treated $Ni_{45}Ti_{50}Cu_5$ (1 – Chang *et al.*[65]), cold rolled and annealed $Ni_{40}Ti_{50}Cu_{10}$ (2 – Nam *et al.*[66], 3 – Lin *et al.*[67]), and annealed $Ni_{40}Ti_{50}Cu_{10}$ wire (4 – Bertacchini *et al.*[68]) samples. (B) Scatter plot of OTR versus peak offset for NiTi, NiTiHf, NiTiPd, and NiTiCu SMAs from literature [27, 29, 31, 32, 52, 55, 69-83]. R-phase martensitic transformations are not included.

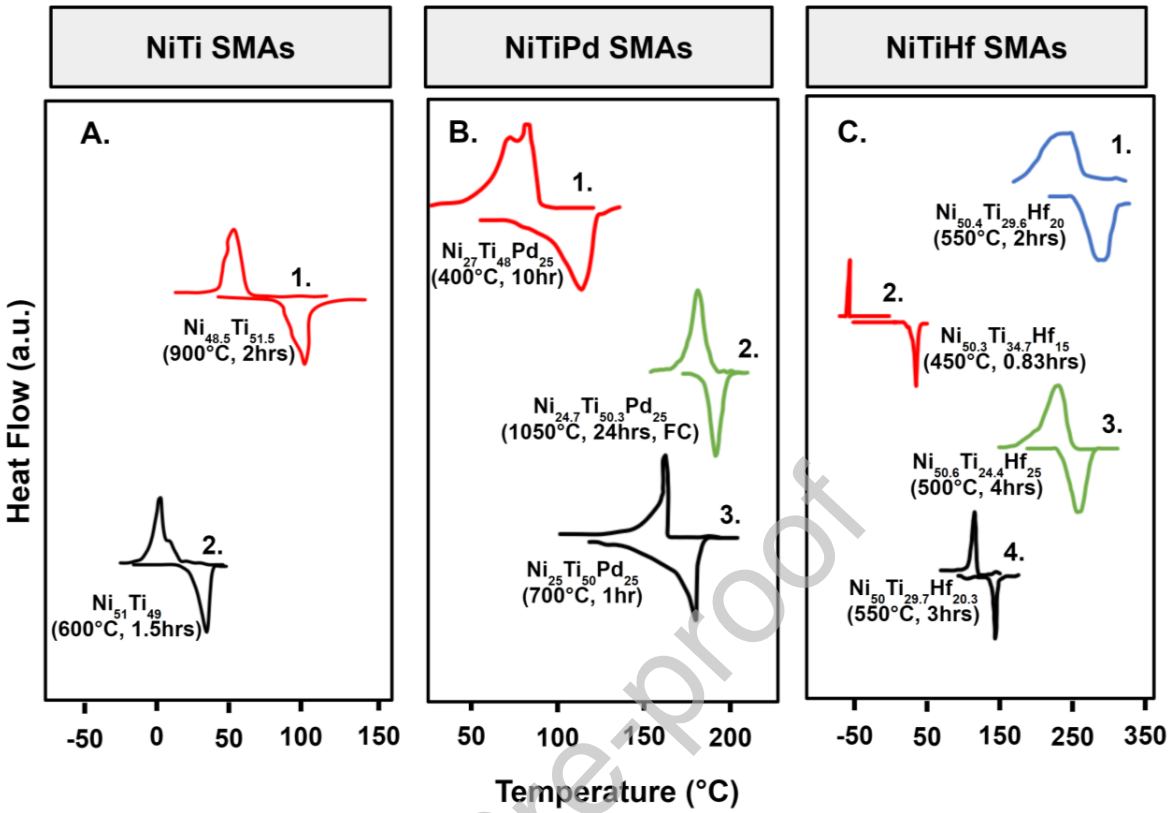

Fig. 3. (A) Adapted DSC plots from NiTi literature for solution annealed $Ni_{48.5}Ti_{51.5}$ (1 – Hsieh *et al.*[84]) and aged $Ni_{51}Ti_{49}$ (2 – Lin *et al.*[82]). (B) Adapted DSC plots from NiTiPd literature for aged $Ni_{27}Ti_{48}Pd_{25}$ (1 – Sasaki *et al.*[85]), solution annealed then furnace cooled $Ni_{24.7}Ti_{50.3}Pd_{25}$ (2 – Ramaiah *et al.*[86]), and aged $Ni_{25}Ti_{50}Pd_{25}$ (3 – Khan *et al.*[79]). (C) Adapted DSC plots from NiTiHf literature for aged $Ni_{50.4}Ti_{29.6}Hf_{20}$ (1 – Meng *et al.*[87]), aged $Ni_{50.3}Ti_{34.7}Hf_{15}$ (2 – Evirgen *et al.*[73]), aged $Ni_{50.6}Ti_{24.4}Hf_{25}$ (3 – Patriarca *et al.*[88]), and aged $Ni_{50}Ti_{29.7}Hf_{20.3}$ (4 – Hornbuckle *et al.*[89]).

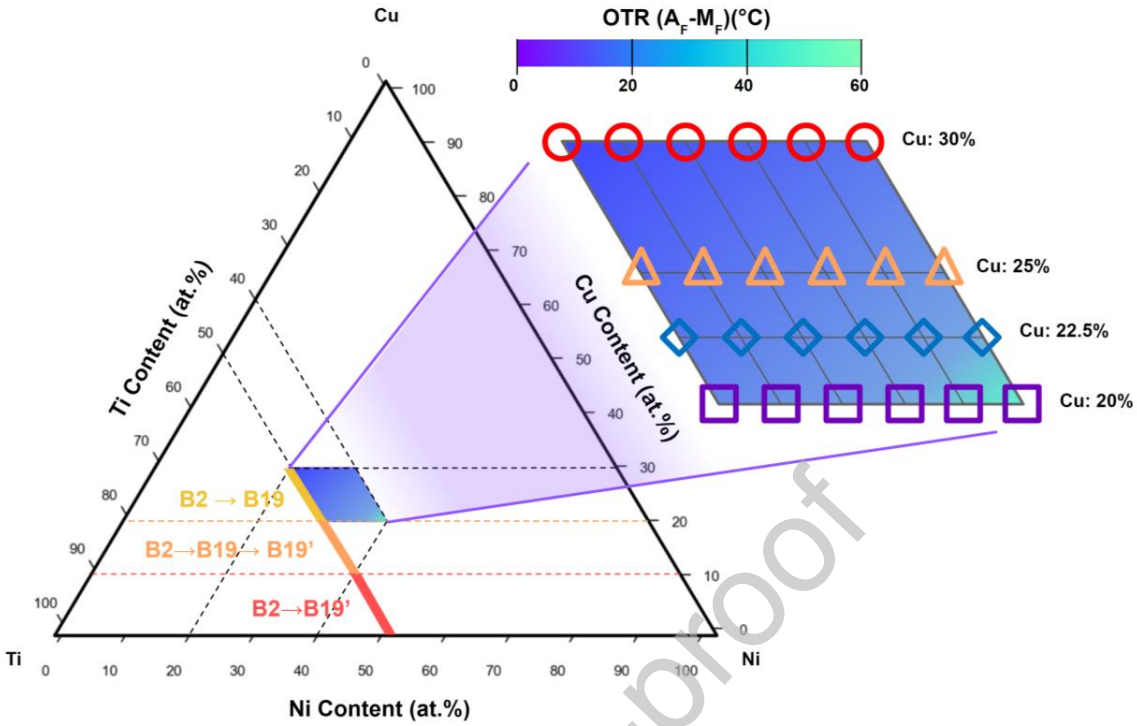

Fig. 4. NiTiCu Ternary Phase Diagram with highlighted grid selected for materials fabrication and testing. Red dashed line at Cu=10 at. % and orange dashed line at Cu=20 at. % separate the composition space into three regions, indicating appearance of single stage B2 (cubic) to B19' (monoclinic) (0 < Cu at. % < 10), two stage B2 to B19 (orthorhombic) to B19' (10 < Cu at. % < 20), and single stage B2-B19 (20 < Cu at. % <30) martensitic transformations[48].

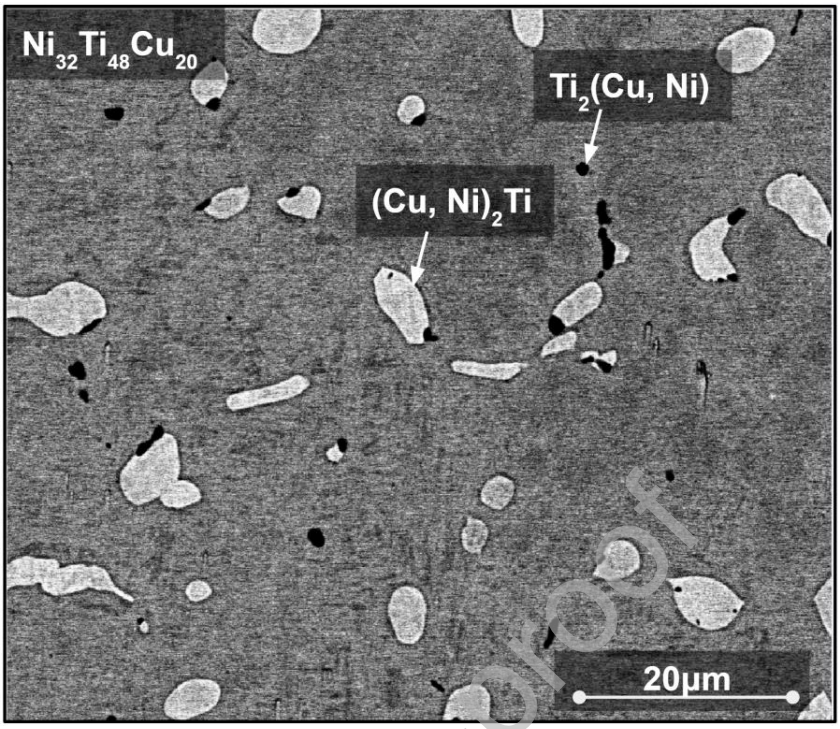

Fig. 5. A representative back scattered electron (BSE) image of a NiTiCu SMA.

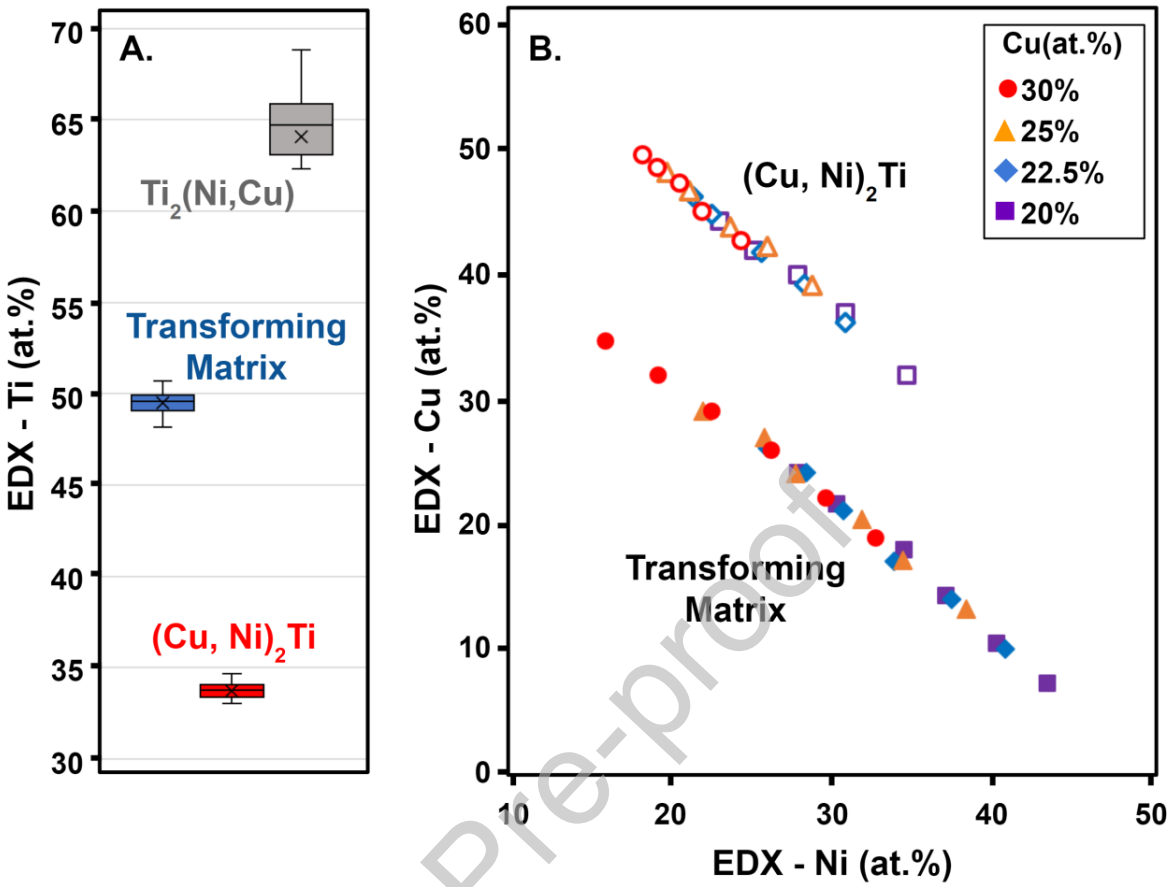

Fig. 6. A) Ti content of the transforming matrix, the second phase, and the black precipitates (see Figure 4) from SEM/EDX imaging. B) The Ni and Cu contents of the transforming matrix and the second phase in each NiTiCu composition studied.

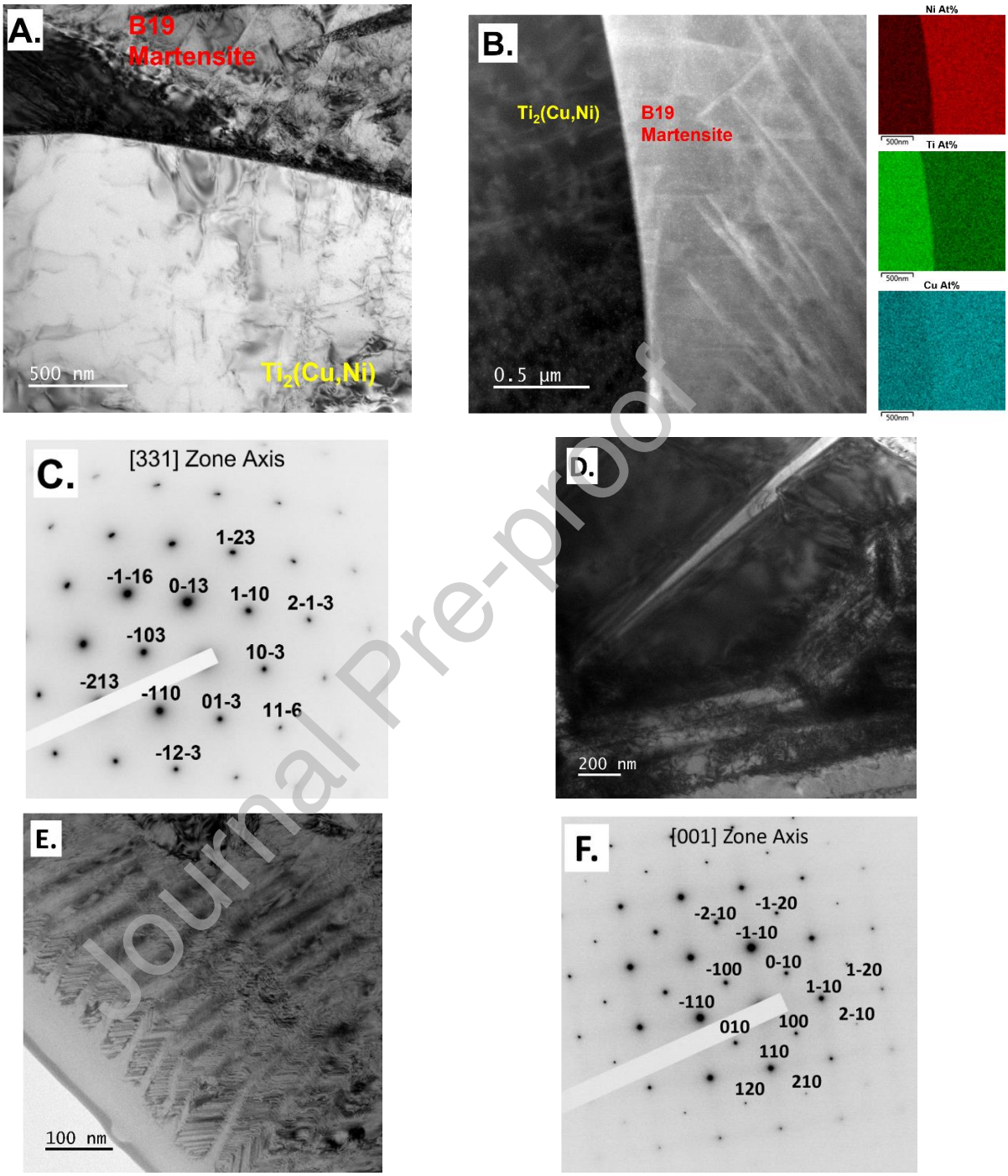

Fig. 7. A) The incoherent interface between B19 martensite and the tetragonal $Ti_2(Cu, Ni)$ second phase in $Ni_{20}Ti_{50}Cu_{30}$, B) EDS composition maps for B19 martensite and $Ti_2(Cu, Ni)$ second phase, C) SADP showing the tetragonal $Ti_2(Cu, Ni)$ second phase with [331] zone axis, D) TEM image showing an average twin spacing of 700 nm in $Ni_{20}Ti_{50}Cu_{30}$, E) Twin spacing of 10 nm in the B19' martensite of binary $Ni_{50.3}Ti$ (wt.%), F) SADP showing the B2 austenite during in-situ heating of $Ni_{20}Ti_{50}Cu_{30}$ to 120 °C.

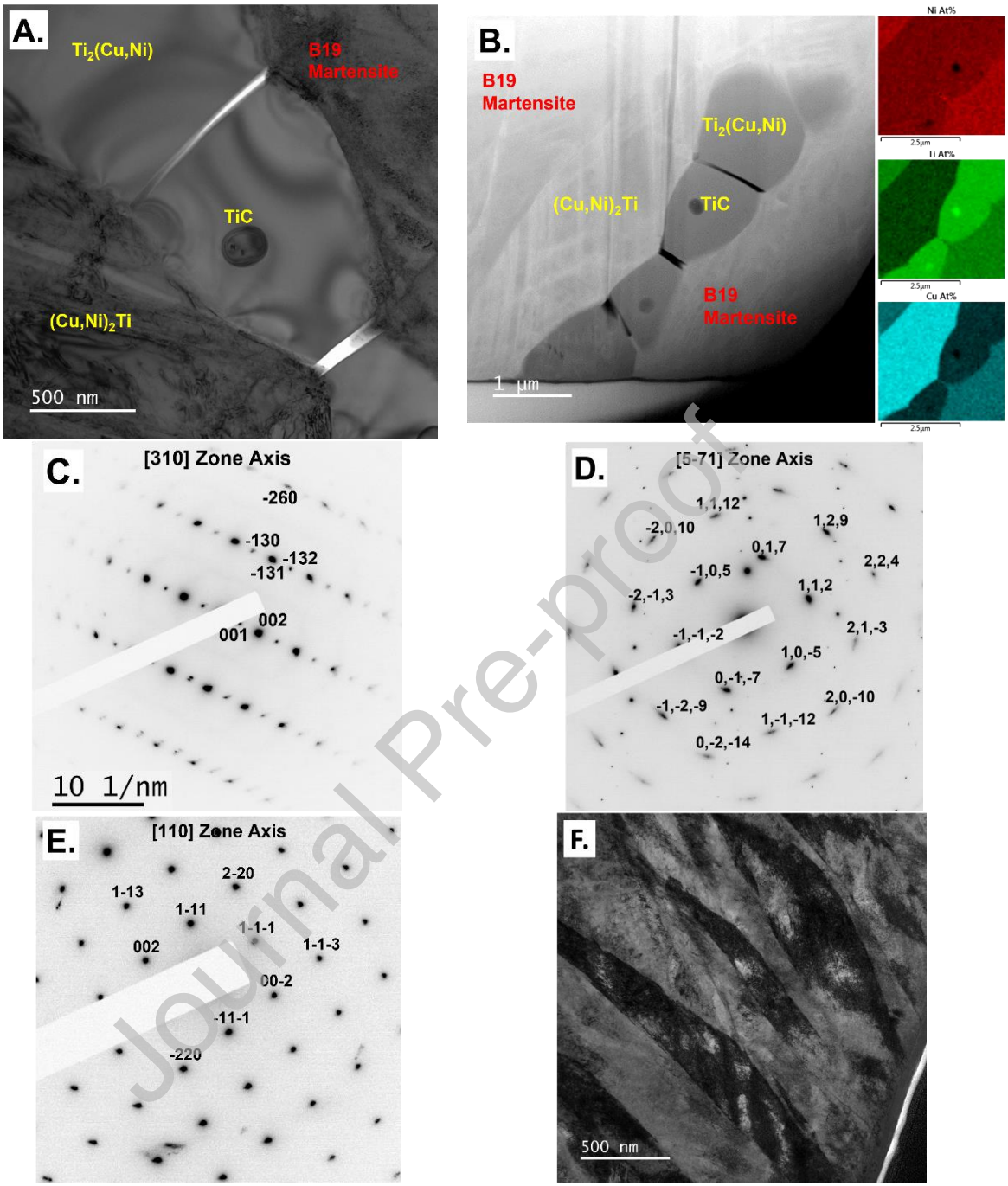

Fig. 8. A) TEM image showing both Ti-rich and Cu-rich second phases, TiC particles and B19 martensite in $Ni_{27}Ti_{48}Cu_{25}$. B) EDS composition maps for both second phases, carbide particles and B19 martensite, C) selected area diffraction pattern (SADP) showing twinned B19 martensite with [310] zone axis, D) SADP with [571] zone axis confirming the Cu-rich second phase as tetragonal $(Cu_{1-x},Ni_x)_2Ti$, E) SADP with [110] zone axis confirming the Ti-rich second phase as cubic $Ti_2(Cu,Ni)$ with the approximate stoichiometry of Ti_6Ni_2Cu, F) TEM image showing an average twin spacing of 280 nm in $Ni_{27}Ti_{48}Cu_{25}$.

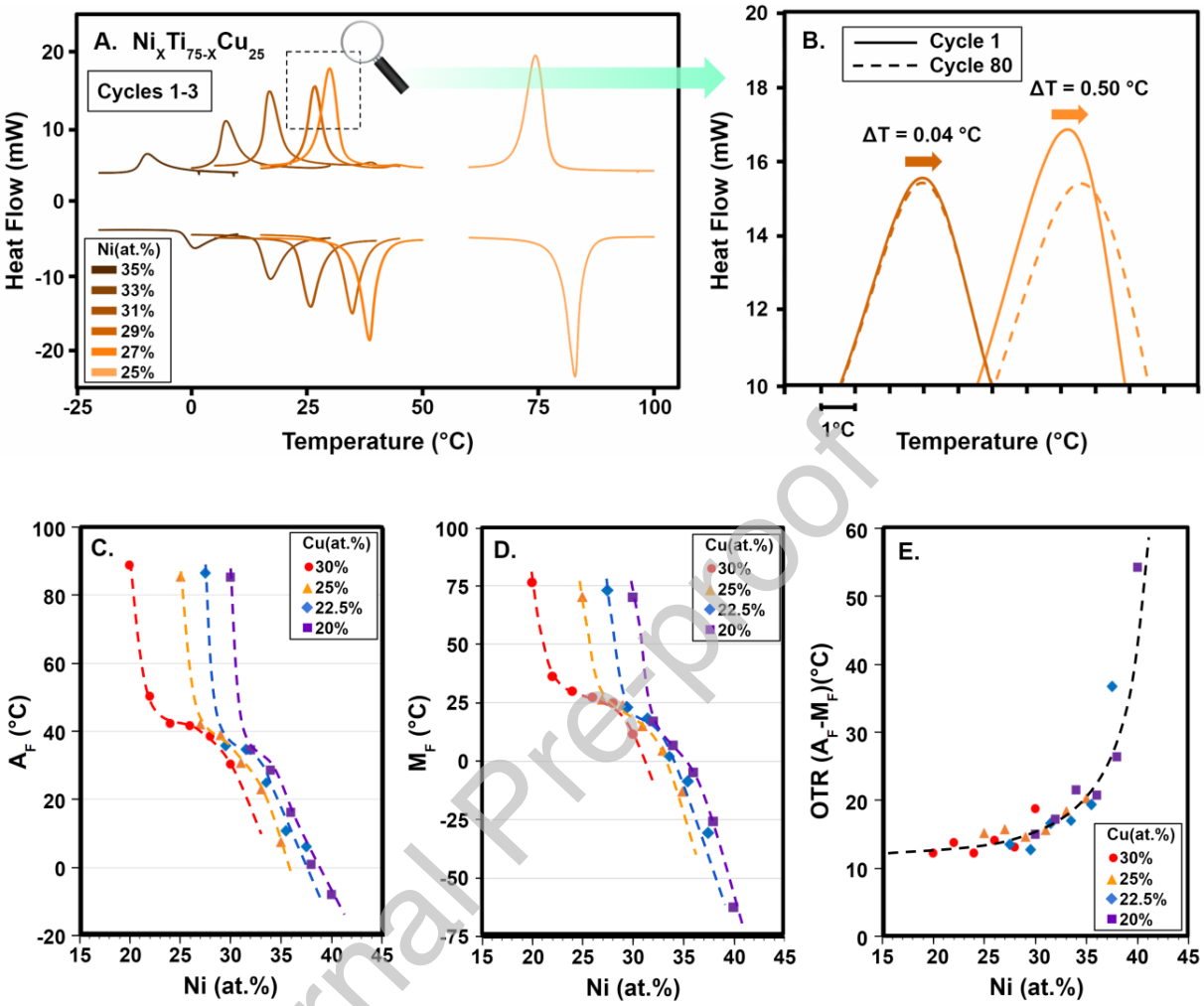

Fig. 9. Differential scanning calorimetry (DSC) results for 3 heating and cooling cycles for $Ni_XTi_{75-X}Cu_{25}$ (A) and a magnified view of the austenite to martensite peaks illustrating excellent thermal cycling stability upon 80 thermal cycles for $Ni_{29}Ti_{46}Cu_{25}$ (left) and $Ni_{27}Ti_{48}Cu_{25}$ (right) (B). All compositions are compared for Austenite Finish (A_F) temperature (C), Martensite Finish (M_F) temperature (D), and OTR (A_F-M_F) (E) with respect to Ni content for NiTiCu SMAs, colored by the Cu content.

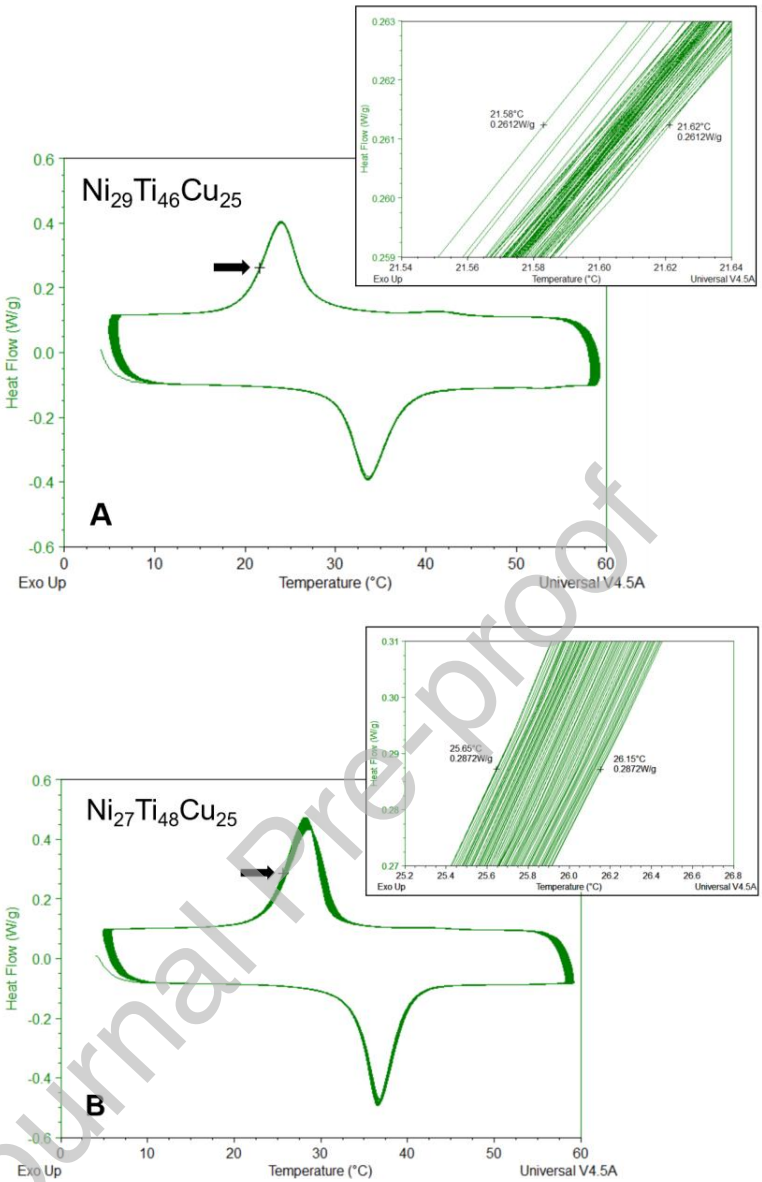

Fig. 10. Cyclic DSC results for $Ni_{29}Ti_{46}Cu_{25}$ (A) and $Ni_{27}Ti_{48}Cu_{25}$ (B) showing 80 thermal cycles. Temperature shift is measured at the midpoint between the maximum and minimum heat flow of the cooling cycle.

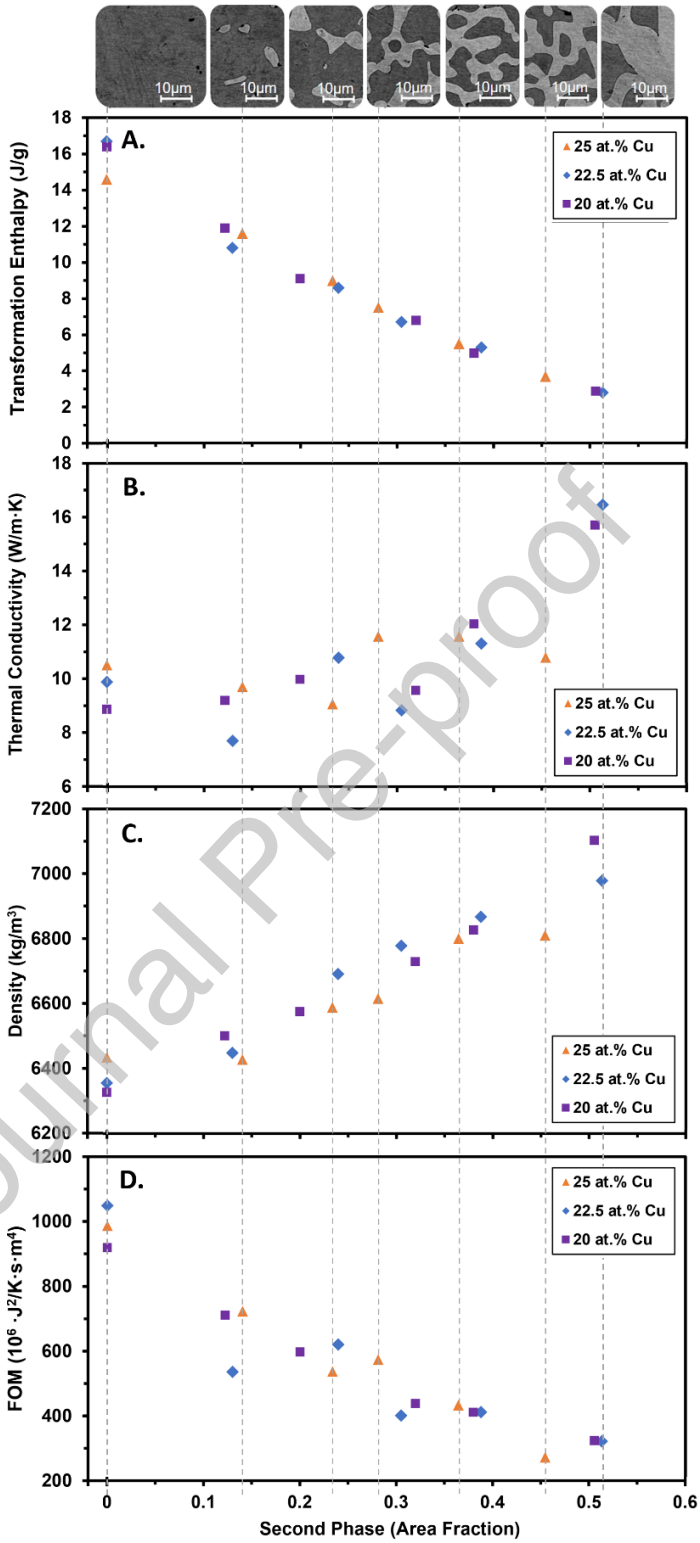

Fig. 11. Transformation enthalpy (A), thermal conductivity (B), density (C), and FOM (D) are plotted against second phase area fraction for NiTiCu alloys of varying composition. Inset images of microstructure show the evolution of second phase. The Ni content generally increases from left to right.

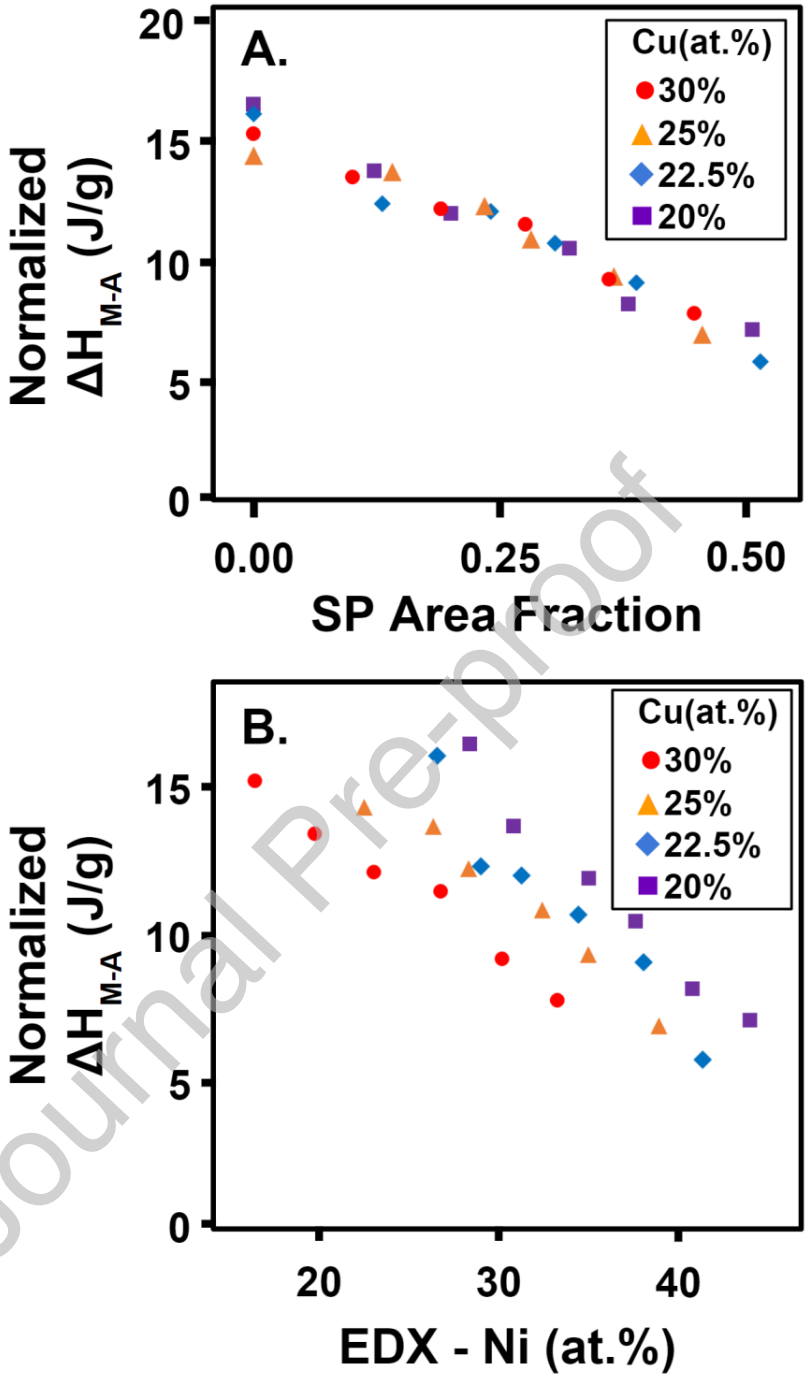

Fig. 12. (A) The normalized latent heat of transformation versus the second phase (SP) area fraction. (B) The normalized latent heat of transformation versus measured Ni content. These figures indicate the cause of the decrease in latent heat is not fully explained by the normalizing the latent heat by the transforming mass.

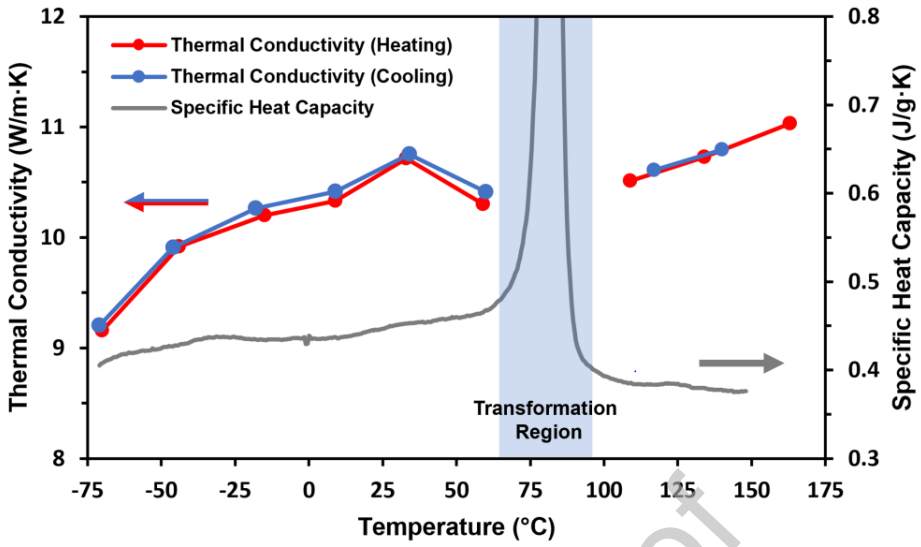

Fig. 13. The thermophysical properties of $Ni_{25}Ti_{50}Cu_{25}$ are plotted as a function of temperature. Thermal conductivity was measured during heating (red) and cooling (blue). Specific heat capacity measured during heating is shown in grey.

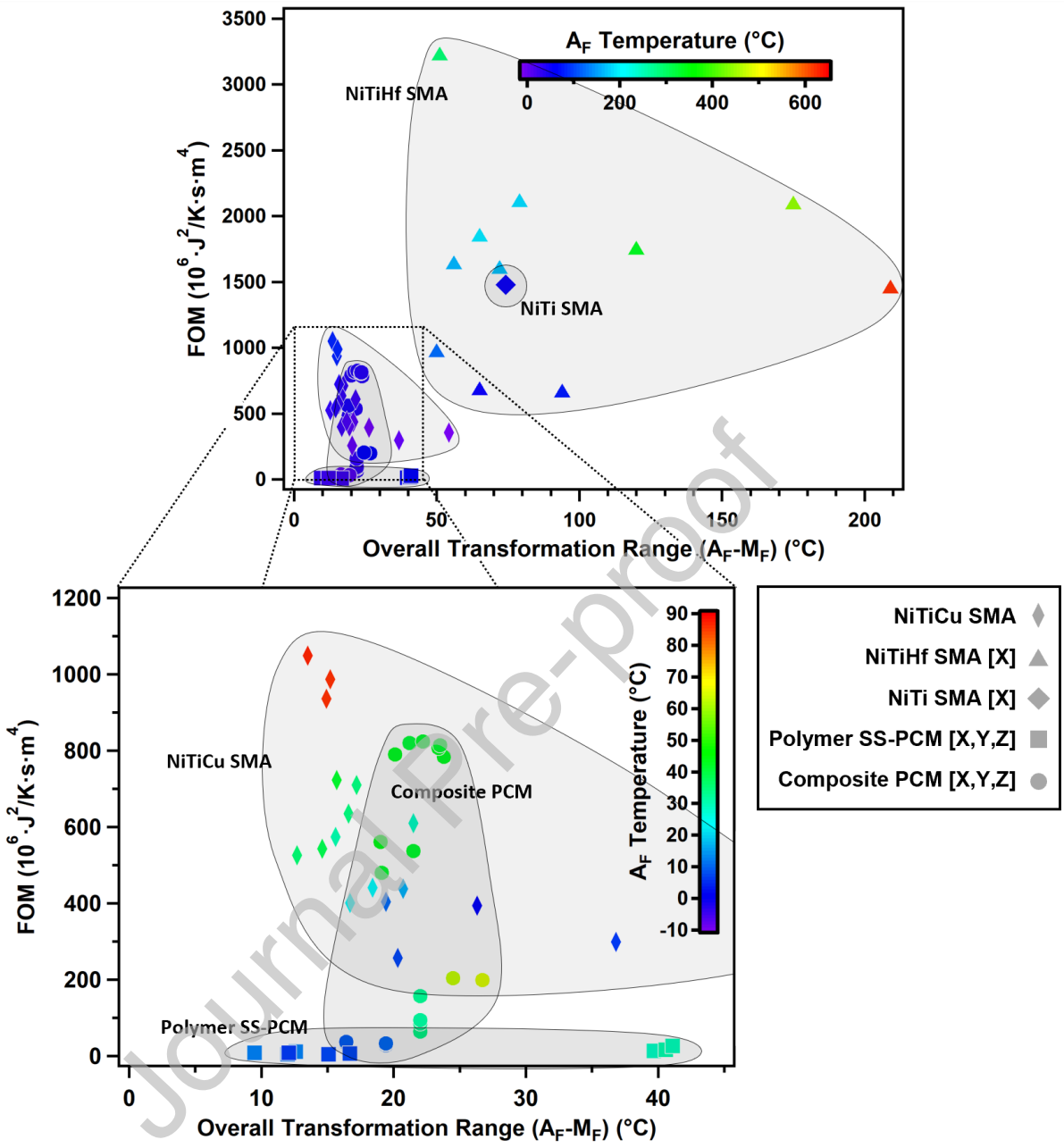

Fig. 14. Figure of Merit (FOM) is plotted against Overall Transformation Range (OTR) for NiTiCu alloys of varying composition in comparison with polymer-based solid-solid Phase Change Materials (PCMs)[62-64], composite PCMs[15-18], NiTiHf SMAs[3], and NiTi SMA[1] for comparison. Material categories are represented by marker shape, and the A_F temperature (melting peak endpoint temperature for traditional PCMs) of each material is represented by marker color. The lower window shows a magnified view of the area inside the dotted outline on the upper window.

LIST of TABLES

Table 1. All compositions presented in this study and their martensitic transformation characteristics with the analyzed Differential Scanning Calorimetry data from the 3rd thermal cycle. This includes transformation temperatures, peak offset (A_s–M_s), OTR (A_f-M_f), thermal hysteresis (A_f-M_s) and the latent heat of transformation for martensite to austenite (ΔH_{MA}) and austenite to martensite (ΔH_{MA}) transformations.

Ni	Ti	Cu	M_f	M_p	M_s	A_s	A_p	A_f	A_s-M_s	A_f-M_f	A_f-M_s	ΔH_{MA}	ΔH_{AM}
at. %			°C									Jg^{-1}	
30.0	40.0	30.0	11.6	15.9	22.3	18.8	22.6	30.3	-3.5	18.7	8	4.0	3.9
28.0	42.0	30.0	25.3	28.0	31.1	30.9	33.6	38.4	-0.2	13.1	7.3	5.6	5.4
26.0	44.0	30.0	27.4	33.3	35.6	34.5	37.7	41.5	-1.1	14.1	5.9	6.8	6.6
24.0	46.0	30.0	30.0	36.5	38.6	38.6	40.3	42.2	0	12.2	3.6	8.8	9.5
22.0	48.0	30.0	36.4	40.5	44.2	42.8	45.3	50.1	-1.4	13.7	5.9	12.0	12.4
20.0	50.0	30.0	76.5	81.1	83.8	83.6	85.6	88.7	-0.2	12.2	4.9	15.5	15.4
35.0	40.0	25.0	-12.8	-9.6	-4.2	-2.1	0.6	7.5	2.1	20.3	11.7	3.5	3.7
33.0	42.0	25.0	4.5	7.9	11.7	14.1	16.6	22.9	2.4	18.4	11.2	5.6	5.5
31.0	44.0	25.0	15.2	17.6	20.8	22.3	24.9	30.8	1.5	15.7	10	7.5	7.5
29.0	46.0	25.0	24.2	27.4	29.7	31.3	33.8	38.8	1.6	14.6	9.1	9.1	9.0
27.0	48.0	25.0	26.2	30.8	32.7	34.9	37.2	41.9	2.2	15.7	9.2	11.6	11.6
25.0	50.0	25.0	70.2	75.5	77.6	79.5	81.5	85.4	1.9	15.2	7.8	14.6	14.6
37.5	40.0	22.5	-30.6	-24.1	-4.5	-18.9	-12.4	6.2	-14.4	36.8	10.7	2.6	2.8
35.5	42.0	22.5	-8.6	-5.5	-0.8	1.6	4.4	10.8	2.4	19.4	11.6	5.2	5.3
33.5	44.0	22.5	6.5	12.1	14.0	14.2	17.4	23.2	0.2	16.7	9.2	6.7	6.7
31.5	46.0	22.5	18.2	21.4	24.5	26.1	29.3	34.8	1.6	16.6	10.3	8.8	8.6
29.5	48.0	22.5	23.0	26.8	28.6	31.5	33.5	35.7	2.9	12.7	7.1	10.6	10.8
27.5	50.0	22.5	73.1	77.9	80.3	81.5	83.7	86.6	1.2	13.6	6.3	16.7	16.7
40.0	40.0	20.0	-62.3	-47.1	-22.2	-49.4	-30.7	-8.1	-27.2	54.2	14.1	3.2	2.9
38.0	42.0	20.0	-25.6	-20.8	-12.1	-13.5	-8.9	0.7	-1.4	26.3	12.8	4.8	5.0
36.0	44.0	20.0	-4.6	-1.6	4.7	4.5	8.4	16.1	-0.2	20.7	11.4	6.8	6.8
34.0	46.0	20.0	6.9	12.8	17.5	16.1	21.3	28.4	-1.4	21.5	10.9	9.3	9.1
32.0	48.0	20.0	17.2	20.7	23.3	26.3	28.8	34.4	3	17.2	11.1	11.9	11.9
30.0	50.0	20.0	70.3	75.5	78.3	79.1	82.5	85.2	0.8	14.9	6.9	16.7	16.4

Declaration of interests

☒ The authors declare that they have no known competing financial interests or personal relationships that could have appeared to influence the work reported in this paper.

☐The authors declare the following financial interests/personal relationships which may be considered as potential competing interests:

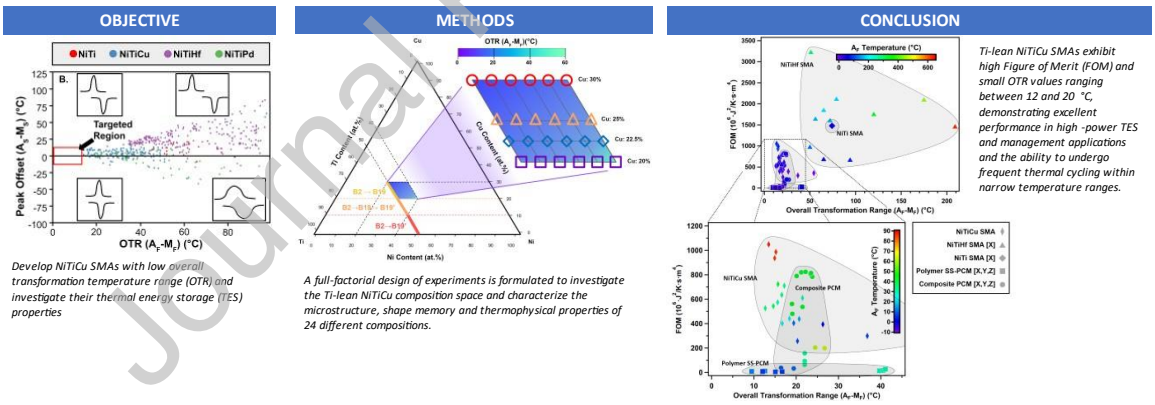

Graphical Abstract